

Three Dimensional Theory of the Ion Channel Laser

Claire Hansel,^{1,*} Agostino Marinelli,^{2,3} Zhirong Huang,^{2,3} and Michael Litos¹

¹*Center for Integrated Plasma Studies, Department of Physics,
University of Colorado Boulder, Boulder, Colorado 80309, USA*

²*Department of Applied Physics, Stanford University, Stanford, California 94305, USA*

³*SLAC National Accelerator Laboratory, Menlo Park, California 94025, USA*

(Dated: September 25th, 2025)

The ion channel laser (ICL) is a plasma-based alternative to the free electron laser (FEL) that uses the electric field of a uniform-density ion channel rather than the magnetic field of an undulator to induce transverse oscillations of electrons in an ultrarelativistic bunch and thereby produce coherent radiation via a collective electromagnetic instability. The powerful focusing of the ion channel generally yields significantly higher gain parameters in the ICL as compared to the FEL. This permits lasing in extremely short distances using electron bunches with an energy spread as large as a few percent; a value readily achievable with current plasma-based accelerators. ICLs, however, impose stringent transverse phase space requirements on the electron bunch beyond what is required in FELs. In this work, we present a novel 3D theory of the planar off-axis configuration of the ICL that accounts for a number of effects including diffraction, transverse radiation profile, frequency and betatron phase detuning, and nonzero spread in energy and undulator parameter. We derive the ICL pendulum and field equations, which we use to write down the 3D Maxwell-Klimontovich equations. After linearizing, we obtain an integro-differential equation describing the z -evolution of the radiation field. The 3D ICL dispersion relation is obtained using a Van Kampen normal mode expansion. We numerically solve the z -evolution equation to compute radiation power growth rates and transverse radiation profiles over a range of different ICL parameters. We examine the gain reduction due to 3D effects, energy spread, and emittance. Electron bunch phase space and emittance requirements for lasing are derived. Finally, we make general observations about the performance and feasibility of the ICL and discuss future prospects.

I. INTRODUCTION

X-ray free electron lasers (XFELs) [1–3] are capable of producing ultrafast, high-brightness, coherent pulses of short-wavelength radiation, making them an invaluable tool across a diverse range of scientific disciplines [4]. However, the significant cost and scale of XFEL facilities limit their utility. The creation of compact laser plasma accelerator (LPA) [5]-driven XFELs has garnered significant research interest [6–10], but despite substantial recent progress [11, 12], such a device has not yet been realized. While LPAs are capable of producing high-energy, high peak-current, low emittance electron beams in a compact footprint, the generally large (order percent) energy spreads exceed the stringent requirements for lasing in an XFEL [6–10]. A number of approaches to overcoming this limitation have been proposed, including beam loading [13], decompression [14, 15], transverse gradient [16] and electromagnetic wave [17] undulators, as well as non-FEL coherent radiation sources [18, 19]. In this work, we focus on different approach: the Ion Channel Laser (ICL) [20–35], a plasma-based alternative to the FEL with extremely high gain and significantly less sensitivity to energy spread.

In an ICL, an electron bunch or laser pulse drives a blowout regime [36] plasma wake in which the light plasma electrons are completely expelled from a region

trailing the driver. Inside this region the stationary heavy plasma ions form a uniform-density ion channel. A trailing electron bunch inside this ion channel experiences a linear transverse focusing force due to the electric field of the ions, which cause the electrons in the bunch to undergo betatron oscillations and emit betatron radiation [7, 27, 28]. The interaction between the trailing bunch and its own betatron radiation causes its structure to change and the radiation to increase exponentially in power and become coherent through a collective electromagnetic instability. While this “ICL instability” is broadly analogous to the FEL instability, there are a number of subtle differences. For example, the equivalent process in the ICL to microbunching in the FEL is more complicated with the sum of the pondermotive and betatron phases bunching rather than just the pondermotive phase. In order for the ICL instability to grow, longitudinal acceleration must be negligible and the beam hosing instability must be mitigated, both of which can be done by using a narrow channel or “wakeless” plasma which can be ionized using electron beam or laser ionization [35, 37]. While in principle either a drive laser or drive bunch could be used to blow out electrons from the plasma and create the ion channel, diffraction and energy depletion would limit the length of an ion channel created with a drive laser to below that needed to saturate in an ICL. The trailing bunch must satisfy certain constraints on emittance (or more accurately, on transverse phase space distribution) and energy spread in order to lase. Compared to the FEL, the ICL has less stringent energy-spread requirements but more stringent emittance

* chansel@slac.stanford.edu

requirements to achieve lasing.

Multiple “configurations” of the ICL are possible depending on the characteristics of the bunch’s phase space distribution. The original literature on the ICL [20–27, 29, 30, 33] considered an “on-axis” configuration where the transverse centroid position of the trailing bunch is in the center of the ion channel and each particle has small transverse normalized momenta ($\gamma\beta_{\perp} \ll 1$), this was shown by Ersfeld *et al.* [31] to require an impractically small emittance to lase. We focus on the more feasible “planar off-axis” configuration [31, 34, 35] where the transverse centroid position of the trailing bunch is initially offset from the ion channel axis which it oscillates around in one plane, and where the bunch spot size is small compared to this offset. While other ICL configurations exist, such as those with circular or elliptical radiation polarization or trailing bunch centroid motion, these are beyond the scope of this paper.

Despite a modest amount of prior literature, much of the fundamental physics of the ICL is poorly understood. This is in large part due to the challenging nature of simulating the ICL. The unique physics of the ICL precludes the use of conventional FEL codes such as GENESIS [38]. While Particle-in-Cell (PIC) codes are able to correctly model the physics, the computational expense of such simulations is generally prohibitive for the ICL. This is because the ICL is a multiscale problem in both the longitudinal (radiation wavelength vs bunch length) and transverse (bunch spot size vs bunch offset) dimensions. In addition, PIC codes can be vulnerable to numerical spacecharge instabilities without special solvers [39] unless performed in the Lorentz boosted frame [40, 41], which introduces its own challenges related to the initialization of fields and particles as well as the process of “unboosting” the numerical diagnostics.

To date, only Davoine *et al.* [34] has managed to simulate the high-gain ICL in 3D, however these simulations are of limited use as they simulated a different, unphysical ICL configuration where circularly polarized radiation interacts with an on-axis cylindrical bunch where particles are initialized with no azimuthal momentum or spread in radial momentum. The existing literature also lacks a comprehensive analytic theory of the ICL. Only Davoine *et al.* considers 3D effects in ICL theory. However, their work is built on assumptions that may limit the theory’s accuracy. In particular, it assumes a particular arbitrary form and width of the transverse radiation profile, ignores the effect of the transverse radiation profile on electron motion, and does not derive the ICL dispersion relation or radiation field z -evolution equation.

In this work, we take a theoretical approach to understanding the 3D physics of the planar off-axis ICL. In Section II, we present a novel analytic theory of the ICL instability and derive equations describing lasing. We introduce numerical methods to solve these equations in Section III which we use in Section IV to obtain radiation power growth rates and transverse radiation profiles. Next, in Section V, we derive the transverse phase

space requirements for lasing. Finally, we discuss the most salient features of our results, their real-world implications, and draw general conclusions about the ICL in Section VI. Throughout this work, we use units of ω_p^{-1} for time, c/ω_p for distance, m_e for mass, $m_e c^2$ for energy, and e for charge, where $\omega_p = (e^2 n_0 / m_e \epsilon_0)^{1/2}$ is the plasma frequency and n_0 is the plasma density.

II. ANALYTIC THEORY

A. Hamiltonian

The Hamiltonian describing a relativistic bunch of N_e electrons traveling down an ion channel is

$$H = \sum_{j=1}^{N_e} \sqrt{1 + (\mathbf{p}_{c,j} + \mathbf{a}(\mathbf{x}_j, t))^2} + \frac{1}{4} \mathbf{x}_{\perp,j}^2 - \phi(\mathbf{x}_j, t) \quad (1)$$

where j is an integer index labeling each electron, $\mathbf{p}_{c,j} = \mathbf{p}_j - \mathbf{a}(\mathbf{x}_j, t)$ is the canonical momentum, $\mathbf{a}(\mathbf{x}, t)$ is the magnetic vector potential, $\phi(\mathbf{x}, t)$ is the electric scalar potential, excluding the $\mathbf{x}_{\perp,j}^2/4$ potential [28] of the ion channel, and \perp refers to the transverse ($\hat{\mathbf{x}}$ and $\hat{\mathbf{y}}$) directions as opposed to the longitudinal ($\hat{\mathbf{z}}$) direction. We can transform Eq. (1) into a more convenient Hamiltonian $\mathcal{H} \equiv H - \sum_{j=1}^{N_e} p_{c,z,j}$ that uses z as the new time variable. Making the paraxial approximation $1 + \mathbf{p}_{\perp,j}^2 \ll \gamma_j^2$, this new Hamiltonian can be written as

$$\mathcal{H} = \sum_{j=1}^{N_e} \frac{1 + (\mathbf{p}_{c,\perp,j} + \mathbf{a}_{\perp}(\mathbf{x}_{\perp,j}, \zeta_j, z))^2}{2\gamma_j} + \frac{1}{4} \mathbf{x}_{\perp,j}^2 - \psi(\mathbf{x}_{\perp,j}, \zeta_j, z) \quad (2)$$

where $\gamma_j = \sqrt{1 + \mathbf{p}_j^2}$ is the Lorentz factor and $\psi \equiv \phi - a_z$ is the wake pseudopotential. The canonical position variables of this new Hamiltonian are x_j , y_j , and $\zeta_j \equiv z - t_j(z)$, and the canonical momentum variables are $p_{c,x,j}$, $p_{c,y,j}$, and H_j . Next, we make two key assumptions. First we assume $\phi_j \ll \gamma_j$, which is equivalent to saying that the electrostatic potential energy due to the bunch charge is much smaller than the electron’s total energy. This is an excellent approximation in practice; for a uniform-density cylindrical bunch with current I the maximum normalized potential is $|I|/I_A$ times a geometric factor of at most a few, where I_A is the Alfvén current which in S.I. units is $I_A = ec/r_e \approx 17$ kA, where r_e is the classical electron radius. Second, we assume $\mathbf{x}_{\perp,j}^2/4 \ll \gamma_j$, implying that the potential energy due to the Coloumb force of the ion column is much smaller than the electron’s total energy. As discussed in Section IIB, this is equivalent to assuming the motion is paraxial and is true for virtually all ICLs. Using these assumptions we

can use $\gamma_j = H_j - \mathbf{x}_{\perp,j}^2/4 + \phi_j \simeq H_j$ instead of H_j as the third canonical momentum variable in Eq. (2).

B. Electron Motion

Next we consider the motion of the electrons in the ion channel in the absence of electromagnetic or bunch spacecharge fields ($\mathbf{a}_{\perp} = \psi = 0$). The equations of motion can be derived from the Hamiltonian in Eq. (2). For now we consider motion entirely in the x - z plane. Solving for the transverse motion gives

$$\begin{aligned} x_j(z) &= a_{\beta,j} \cos(k_{\beta,j}z + \varphi_j) \\ p_{x,j}(z) &= -K_j \sin(k_{\beta,j}z + \varphi_j) \end{aligned} \quad (3)$$

where $a_{\beta,j}$ is the betatron oscillation amplitude, $k_{\beta,j} = 1/\sqrt{2}\gamma_j$ is the betatron angular wavenumber, φ_j is the initial phase at $z = 0$, and

$$K_j = \gamma_j k_{\beta,j} a_{\beta,j} \quad (4)$$

is the undulator parameter. In Section II A we assumed $\mathbf{x}_{\perp,j}^2/4 \ll \gamma_j$. Here we see this is equivalent to the assumption $K_j^2 \ll \gamma_j^2$ which is equivalent to the paraxial assumption $p_{x,j}^2 \ll \gamma_j^2$. For ICLs with very low energies and large transverse offsets, this assumption can be violated leading to relativistic effects causing the betatron oscillations to become anharmonic [28]. While we consider this extreme regime to be beyond the scope of this work, we note it has been investigated by Frazzitta *et al.* [42]. The two longitudinal equations can be solved to give

$$\begin{aligned} \zeta_j(z) &= \zeta_{0,j} - \frac{1 + \frac{K_j^2}{2}}{2\gamma_j^2} z - \frac{K_j^2}{8\gamma_j^2 k_{\beta,j}} \sin(2\varphi_j) \\ &\quad + \frac{K_j^2}{8\gamma_j^2 k_{\beta,j}} \sin(2(k_{\beta,j}z + \varphi_j)) \\ \gamma_j(z) &= \gamma_j \end{aligned} \quad (5)$$

where $\zeta_{0,j}$ and γ_j are constants. Unlike in an undulator where $\gamma_j(z)$ is truly constant since static magnetic fields do no work, in an ion channel $\gamma_j(z)$ is only approximately constant; the paraxial approximation allows us to ignore the z dependent subleading term which is oscillatory with amplitude of order K_j^2/γ_j . Each electron in an ICL emits $\hat{\mathbf{z}}$ directed betatron radiation at a fundamental wavelength $\lambda_{1,j}$ equal to the distance behind a particle moving the speed of light the electron slips during one oscillation period. Mathematically, $-\lambda_{1,j} = \zeta_j(z + \lambda_{\beta,j}) - \zeta_j(z)$, where $\lambda_{\beta,j} = 2\pi/k_{\beta,j}$ is the betatron wavelength. Using Eq. (5), this yields the ICL resonance condition

$$\lambda_{1,j} = \lambda_{\beta,j} \frac{1 + \frac{K_j^2}{2}}{2\gamma_j^2}. \quad (6)$$

For $K_j \gtrsim 1$, radiation is also emitted at odd harmonics $\lambda_{h,j} = \lambda_{1,j}/h$ where h is an odd integer.

As discussed in the introduction, in this paper we consider only the planar off-axis ICL configuration. In this configuration, the fictitious ideal ‘‘reference particle’’ oscillates entirely in the x - z plane with motion given by Eqs. (3) and (5). However, because we aim to include the effect of nonzero emittance in our theory, we must contend with the fact that in general, particles in the bunch do not oscillate strictly in this plane. For general non-planar motion, the trajectories of electrons in the ion channel are elliptical helices. We call the ellipse traced out in the x - y plane during this motion the orbit ellipse. These electrons have oscillation amplitudes in both dimensions ($a_{\beta,x,j}$ and $a_{\beta,y,j}$) as well as undulator parameters in both dimensions ($K_{x,j}$ and $K_{y,j}$). By computing $\zeta_j(z)$ it can be shown that the resonance condition Eq. (6) also holds in the non-planar case, provided the ‘‘radial’’ undulator parameter $K_j \equiv \sqrt{K_{x,j}^2 + K_{y,j}^2}$ is used. While planar transverse motion is parameterized by only two quantities, the undulator parameter K_j and the oscillation phase φ_j , non-planar transverse motion is parameterized by four quantities: the undulator parameter K_j , the oscillation phase φ_j , the orientation angle of the orbit ellipse (angle between the x axis and the semimajor axis), and the eccentricity angle of the orbit ellipse (arctangent of the aspect ratio). When a nonzero emittance bunch enters an ion channel, the spread in $(x_j, y_j, p_{x,j}, p_{y,j})$ can be expressed as a spread in these four parameters. Of these four parameters, only the undulator parameter K_j appears in the equation Eq. (6) for the fundamental wavelength $\lambda_{1,j}$. The spread in $\lambda_{1,j}$, which is determined by the spread in K_j due to nonzero emittance along with the energy spread, must satisfy $\Delta\lambda_1/\lambda_1 \lesssim \rho$ for lasing as discussed in Section V, where ρ is the gain parameter, including any 3D or finite emittance or energy spread effects, defined in terms of the power gain length, *i.e.* the propagation length required to produce an e -fold increase in radiation power:

$$L_G = \frac{\lambda_{\beta,r}}{4\pi\sqrt{3}\rho}. \quad (7)$$

As $\Delta\lambda_1/\lambda_1$ approaches ρ , the ICL radiation power growth rate decreases until eventually the ICL instability is stabilized. This is the fundamental constraint from which the ICL emittance and energy spread requirements arise. While spread in orientation and eccentricity angle of the orbit ellipses in the bunch do not lead to spread in fundamental wavelength, they do still decrease the ICL gain. Electrons with very different orbit ellipses couple less efficiently to each others’ emitted radiation and produce radiation with different polarizations leading to some destructive interference. These effects directly decrease ρ . However, because we consider bunches with spot size much smaller than their transverse offset, the amount these effects decrease the ICL is negligible. Moving forward, we ignore these effects by approximating the

motion of the bunch electrons as being entirely in the x - z plane and described by Eqs. (3) and (5), with the caveat that K_j is understood to be the *radial* undulator parameter rather than simply $K_{x,j}$. This distinction is important for example in Section V when computing ΔK .

It is illuminating to make a comparison here to the FEL. In both the FEL and ICL, $\Delta\lambda_1/\lambda_1 \lesssim \rho$ is the fundamental constraint from which both the emittance and energy spread constraints arise [43]. However, the way in which a bunch's emittance causes a spread in radiation wavelength $\Delta\lambda_1$ differs between the two. In the FEL, the undulator period averaged electron motion is simply a constant velocity motion at some small angle $\theta_{\beta,j}$ with respect to the \hat{z} direction. Since the undulator radiation is emitted at this angle, the component of this radiation projected along the \hat{z} -direction has a shifted frequency. The FEL resonance condition is $\lambda_{1,j} = (\lambda_u/(2\gamma_j^2))(1 + K_u^2/2 + \gamma_j^2\theta_{\beta,j}^2)$ (S.I.) where λ_u is the undulator period, $K_u = e\lambda_u B_0/(2\pi m_e c)$ (S.I.) is the undulator parameter, and B_0 is the undulator magnetic field strength. When a nonzero emittance bunch enters an FEL, the spread in $(x_j, y_j, p_{x,j}, p_{y,j})$ due to its emittance leads to a spread in the angle $\theta_{\beta,j}$ at which radiation is emitted, leading to a spread in fundamental wavelength. The undulator parameter K_u is the same for each electron and makes no contribution to the spread in fundamental wavelength. In contrast, in the ICL the betatron period averaged motion of every electron points exactly along the \hat{z} axis of the ion channel. There is no angular spread in the direction of the emitted radiation, and the spread in fundamental wavelengths $\Delta\lambda_1$ is entirely due to the spread in K_j .

C. Pendulum Equations

To derive the pendulum equations we adopt the following approach broadly similar to existing FEL theory [1]. Previously we solved for the electron motion in the absence of the radiation fields obtaining Eqs. (3) and (5) for the evolution of the four coordinates $(x_j, p_{x,j}, \zeta_j, \gamma_j)$ in terms of z and four constants $(K_j, \varphi_j, \zeta_{0,j}, \gamma_j)$. In this section we turn those fields back on and let the motion be described by these same equations, except with the four constants now allowed to vary with z . Next we construct four ‘‘pendulum quantities’’ defined in terms of $(K_j, \varphi_j, \zeta_{0,j}, \gamma_j)$ and z that vary slowly over a single betatron oscillation. After inverting Eqs. (3) and (5) and rewriting the pendulum quantities in terms of $(x_j, p_{x,j}, \zeta_j, \gamma_j)$ and z , we use the equations of motion derived from the Hamiltonian in Eq. (2) to compute the (unaveraged) pendulum equations describing the z evolution of the pendulum quantities. After simplifying these equations by ignoring terms we can show are small, we average these equations over the betatron oscillation period to obtain the period-averaged pendulum equations, which are the main result of this subsection.

The four pendulum quantities we choose are

$$\begin{aligned} \eta_j &\equiv \frac{\gamma_j - \gamma_r}{\gamma_r} \\ \delta_j &\equiv \frac{K_j - K_r}{K_r} \\ \theta_j &\equiv k_{\beta,r}z + k_{1,r} \left(\zeta_{0,j} - \frac{1 + \frac{K_j^2}{2}}{2\gamma_j^2} z \right. \\ &\quad \left. - \frac{K_j^2}{8\gamma_j^2 k_{\beta,j}} \sin(2\varphi_j) \right) \\ \vartheta_j &\equiv \varphi_j + k_{\beta,j}z - k_{\beta,r}z \end{aligned} \quad (8)$$

where the z -dependence of $(\eta_j, \delta_j, \theta_j, \vartheta_j)$ and $(K_j, \varphi_j, \zeta_{0,j}, \gamma_j)$ is implicit and the subscript r refers to the reference value of a quantity which does not depend on z or the particle index j . The parameters η_j and θ_j are the energy detuning and pondermotive phase which are defined in the same way as in FEL theory [1]. It is important to note that in the definition of θ_j the reference value—rather than the individual particle values—of k_β and k_1 are used, since θ_j is not only a quantity defined for each particle, but also a field coordinate $\theta(z, \zeta) \equiv k_{\beta,r}z + k_{1,r}\zeta$ used in the field equation in Section IID. The parameters δ_j and ϑ_j are the undulator parameter detuning and the betatron phase detuning respectively. These are unique to ICL theory and not found in FEL theory. In the off-axis configuration of the ICL the bunch spot size is small compared to the centroid offset and so the spread in K_j is small. Since we also assume small energy spread, $\eta_j, \delta_j \ll 1$. It is important to note that the pendulum quantities in Eq. (8) are chosen somewhat arbitrarily. We could have, for example, instead used $a_{\beta,j}$, K_j^2 , or $\lambda_{1,j}$ detuning.

Having defined the pendulum quantities, we now derive the pendulum equations. By inverting Eqs. (3) and (5) to give $(K_j, \varphi_j, \zeta_{0,j}, \gamma_j)$ in terms of $(x_j, p_{x,j}, \zeta_j, \gamma_j)$ and substituting these into Eq. (8), we can write the pendulum quantities in terms of the four coordinates $(x_j, p_{x,j}, \zeta_j, \gamma_j)$ and z

$$\begin{aligned} \eta_j &= \frac{\gamma_j - \gamma_r}{\gamma_r} \\ \delta_j &= \frac{\sqrt{p_{x,j}^2 + \gamma_j^2 k_{\beta,j}^2 x_j^2} - K_r}{K_r} \\ \theta_j &= k_{\beta,r}z + k_{1,r}\zeta_j + \frac{k_{1,r}x_j p_{x,j}}{4\gamma_j} \\ \vartheta_j &= \text{atan2}(-p_{x,j}, \gamma_j k_{\beta,j} x_j) - k_{\beta,r}z. \end{aligned} \quad (9)$$

Next, we take the z derivative of the pendulum parameters in Eq. (9) and substitute first the equations of motion obtained from the Hamiltonian in Eq. (2) and then Eqs. (3) and (5) for the four coordinates to obtain the unaveraged pendulum equations

$$\begin{aligned}
\eta'_j &= \frac{K_j}{\gamma_r \gamma_j} \sin(k_{\beta,j} z + \varphi_j) \left. \frac{\partial a}{\partial \zeta} \right|_j + \frac{1}{\gamma_r} \left. \frac{\partial \psi}{\partial \zeta} \right|_j \\
\delta'_j &= \frac{1 + K_j^2}{2\gamma_j^2 K_r} \sin(k_{\beta,j} z + \varphi_j) \left. \frac{\partial a}{\partial \zeta} \right|_j - \frac{1}{K_r} \sin(k_{\beta,j} z + \varphi_j) \left. \frac{\partial a}{\partial z} \right|_j + \frac{K_j}{2\gamma_j K_r} \cos^2(k_{\beta,j} z + \varphi_j) \left. \frac{\partial \psi}{\partial \zeta} \right|_j \\
\theta'_j &= k_{\beta,r} - k_{1,r} \frac{1 + \frac{K_j^2}{2}}{2\gamma_j^2} - \frac{k_{1,r} k_{\beta,j} K_j \cos(k_{\beta,j} z + \varphi_j)}{2\gamma_j} \left(\frac{1 - K_j^2 \sin^2(k_{\beta,j} z + \varphi_j)}{2\gamma_j^2} \left. \frac{\partial a}{\partial \zeta} \right|_j - \left. \frac{\partial a}{\partial z} \right|_j \right) \\
&\quad + \frac{k_{1,r} k_{\beta,j} K_j^2}{4\gamma_j^2} \sin(2(k_{\beta,j} z + \varphi_j)) \left. \frac{\partial \psi}{\partial \zeta} \right|_j \\
\vartheta'_j &= k_{\beta,j} - k_{\beta,r} + \frac{1}{2\gamma_j^2 K_j} \cos(k_{\beta,j} z + \varphi_j) \left. \frac{\partial a}{\partial \zeta} \right|_j - \frac{1}{K_j} \cos(k_{\beta,j} z + \varphi_j) \left. \frac{\partial a}{\partial z} \right|_j - \frac{1}{4\gamma_j} \sin(2(k_{\beta,j} z + \varphi_j)) \left. \frac{\partial \psi}{\partial \zeta} \right|_j
\end{aligned} \tag{10}$$

where a refers to the $\hat{\mathbf{x}}$ component of the field $\mathbf{a}(\mathbf{x}_\perp, \zeta, z)$, and $|_j$ refers to evaluation at $\mathbf{x}_\perp = \mathbf{x}_{\perp,j}(z)$, $\zeta = \zeta_j(z)$. Additionally, in Eq. (10) we neglected transverse spacecharge fields (which are a factor of γ smaller than the longitudinal spacecharge fields) by ignoring the transverse derivatives of ψ .

Eq. (10) can be simplified considerably, and the four pendulum parameters can be shown to vary slowly over one betatron period by making order of magnitude arguments about the various terms. The orders of magnitude of the various quantities can be derived from the normalization used later on in Section II E and are $\partial_\zeta \sim h k_{1,r}$, $\partial_z \sim L_G^{-1}$, $\delta_j, \eta_j \lesssim \rho \ll 1$, $L_p \lesssim 40 L_G$, and $a \lesssim \rho^2 / (2\xi_r [\text{JJ}]_h)$ where L_p is the plasma length, h is the integer harmonic number, $[\text{JJ}]_h \equiv J_{(h-1)/2}(h\xi_r) - J_{(h+1)/2}(h\xi_r)$ where J is the Bessel function of the first kind, and $\xi_r \equiv K_r^2 / (2(2 + K_r^2))$. The second term in the δ'_j equation can be neglected, since it is subleading, and the terms in the θ'_j and ϑ'_j equations that depend on a can be shown to change θ_j and φ_j respectively by an amount much less than unity over the length of the plasma. While making these order-of-magnitude arguments we assume the harmonic number is no larger than a few and $K \gtrsim 1$. As discussed further in Section II E, an ICL with $K \lesssim 1$ is impractical due to diffraction.

Finally, while we have included the effect of longitudinal spacecharge up to this point, we ignore it going forward by setting longitudinal derivatives of ψ to zero. This is also done in Davoine *et al.* [34], and we refer to the justification used there which says longitudinal spacecharge can be ignored when $k_{p,b} L_{G,0} \lesssim 1$ where $k_{p,b} = \sqrt{n_b / (\gamma^3 n_0)}$ is the beam's plasma angular wavenumber and $L_{G,0}$ is the cold 1D gain length defined in Section II E. After writing γ_j and K_j in terms of their respective reference values and detunings, and ignoring subleading order terms in η_j and δ_j , we arrive at

$$\begin{aligned}
\eta'_j &= \frac{K_r}{\gamma_r^2} \sin(k_{\beta,r} z + \vartheta_j) \left. \frac{\partial a}{\partial \zeta} \right|_j \\
\delta'_j &= \frac{1 + K_r^2}{2K_r^2} \eta'_j \\
\theta'_j &= 2k_{\beta,r} \left(\eta_j - \frac{K_r^2}{2 + K_r^2} \delta_j \right) \\
\vartheta'_j &= -\frac{1}{2} k_{\beta,r} \eta_j
\end{aligned} \tag{11}$$

where we have also rewritten the argument of the sine function in the first equation using the definition of ϑ_j from Eq. (8).

The next step is to period average Eq. (11) according to the definition of the period average in Appendix A. The δ'_j , θ'_j , and ϑ'_j pendulum equations do not change when period averaged since they contain only slowly varying quantities, but the η'_j equation is nontrivial. We make the slowly varying envelope approximation as described in Appendix C. Using Eqs. (C2) and (C3), the period averaged η'_j equation is

$$\begin{aligned}
\eta'_j &= \sum_{h \in \mathbb{N}^+} \int_{\nu \approx h} d\nu \frac{i\nu k_{1,r} K_r}{\gamma_r^2} \overline{\mathcal{A}_h(\mathbf{x}_{\perp,j}(z), \nu, z)} \\
&\quad \times \overline{\sin(k_{\beta,r} z + \vartheta_j) e^{i\nu k_{1,r} \zeta_j(z)} e^{i\Delta\nu k_{\beta,r} z} + \text{c.c.}}
\end{aligned} \tag{12}$$

In the FEL, the transverse undulator oscillation amplitude $a_{u,j} \equiv K_u / (\gamma_j k_u)$ is always small compared to the transverse radiation size, and so particles oscillate locally in a small part of the radiation field. This means that the field can be treated as effectively constant over an oscillation period and when computing the period average of the η'_j equation, $\mathcal{A}_h(\mathbf{x}_{\perp,j}(z), \nu, z)$ is slowly varying and can be taken out of the period average. In the ICL, however, $a_{\beta,j}$ is the same order as the transverse radiation size, which means electrons oscillate in and out of the core of the radiation field every oscillation. Even though $\mathcal{A}_h(\mathbf{x}_\perp, \nu, z)$ is slowly varying, $\mathcal{A}_h(\mathbf{x}_{\perp,j}(z), \nu, z)$ is not and can't necessarily be taken out of the period average in Eq. (12). Despite this, it

still is possible to compute the period average for arbitrary transverse mode shape by performing a Fourier transform of the field in the transverse plane, period averaging, and then performing an inverse Fourier transform. This is equivalent to using a delta function to write $\mathcal{A}_h(\mathbf{x}_\perp, j(z), \nu, z) = \int d^2\mathbf{x}_\perp \mathcal{A}_h(\mathbf{x}_\perp, \nu, z) \delta^2(\mathbf{x}_\perp - \mathbf{x}_{\perp, j}(z))$ and then taking the slowly varying $\mathcal{A}_h(\mathbf{x}_\perp, \nu, z)$ out of the period average.

Using this procedure along with the result Eq. (A6) from Appendix A, we can period average Eq. (12). Combining this with the other three period averaged pendulum equations which are the same as their unaveraged forms from Eq. (11), we can write down the period averaged pendulum equations

$$\begin{aligned} \eta'_j &= \sum_{h \in \mathbb{N}^+} \int_{\nu \approx h} d\nu \frac{\nu k_{1,r} K_r [\text{JJ}]_h}{2\gamma_r^2} e^{ih\vartheta_j} e^{i\nu\theta_j} \\ &\quad \times \int d^2\mathbf{x}_\perp \mathcal{W}_h(\mathbf{x}_\perp) \mathcal{A}_h(\mathbf{x}_\perp, \nu, z) + \text{c.c.} \\ \delta'_j &= \frac{1 + K_r^2}{2K_r^2} \eta'_j \\ \theta'_j &= 2k_{\beta,r} \left(\eta_j - \frac{K_r^2}{2 + K_r^2} \delta_j \right) \\ \vartheta'_j &= -\frac{1}{2} k_{\beta,r} \eta_j \end{aligned} \quad (13)$$

where $\mathcal{W}_h(\mathbf{x}_\perp)$ is defined in Eq. (A7) and $[\text{JJ}]_h$ is defined in Eq. (A8).

D. Field Equation

In this section, we derive the period averaged field equation for $\mathcal{A}_h(\mathbf{x}_\perp, \nu, z)$. The field equation in Lorentz gauge for the $\hat{\mathbf{x}}$ component of the magnetic vector potential with a source term due to the N_e electrons in the bunch is

$$\begin{aligned} \left[\frac{\partial^2}{\partial t^2} - \nabla^2 \right] a(\mathbf{x}, t) &= \\ - \frac{4\pi}{I_A} \sum_{j=1}^{N_e} \frac{dx_j(t)}{dt} \delta^3(\mathbf{x} - \mathbf{x}_j(t)). \end{aligned} \quad (14)$$

We transform coordinates from (z, t) to (ζ, z) and make the slowly varying envelope approximation ($\partial_z \ll \partial_\zeta$) as discussed in Appendix C to obtain

$$\begin{aligned} \left[\frac{\partial^2}{\partial z \partial \zeta} + \frac{1}{2} \nabla_\perp^2 \right] a(\mathbf{x}_\perp, \zeta, z) &= \\ \frac{2\pi}{I_A} \sum_{j=1}^{N_e} x'_j(z) \delta^2(\mathbf{x}_\perp - \mathbf{x}_{\perp, j}(z)) \delta(\zeta - \zeta_j(z)). \end{aligned} \quad (15)$$

Next, we Fourier transform using Eq. (C1) and use the

definition of $\mathcal{A}_h(\mathbf{x}_\perp, \nu, z)$ from Eq. (C3) to get

$$\begin{aligned} \left[\frac{\partial}{\partial z} + i\Delta\nu k_{\beta,r} - \frac{i}{2\nu k_{1,r}} \nabla_\perp^2 \right] \mathcal{A}_h(\mathbf{x}_\perp, \nu, z) &= \\ \frac{e^{-i\Delta\nu k_{\beta,r} z}}{i\nu I_A} \sum_{j=1}^{N_e} x'_j(z) \delta^2(\mathbf{x}_\perp - \mathbf{x}_{\perp, j}(z)) e^{-i\nu k_{1,r} \zeta_j}. \end{aligned} \quad (16)$$

The left-hand side of the above equation is unchanged by period averaging. The period average of the source term can be computed by substituting in $x'_j(z)$, which can be obtained from Eq. (3) and using Eq. (A6). The result is

$$\begin{aligned} \left[\frac{\partial}{\partial z} + i\Delta\nu k_{\beta,r} - \frac{i}{2\nu k_{1,r}} \nabla_\perp^2 \right] \mathcal{A}_h(\mathbf{x}_\perp, \nu, z) &= \\ - \frac{K_r [\text{JJ}]_{h,r}}{2\nu I_A \gamma_r} \mathcal{W}_h(\mathbf{x}_\perp) \sum_{j=1}^{N_e} e^{-i\nu\theta_j} e^{-ih\vartheta_j} \end{aligned} \quad (17)$$

which is the period-averaged field equation and the main result of this section.

In the source term on the right hand side of Eq. (17) is a bunching factor $\sum_{j=1}^{N_e} e^{-i(\nu\theta_j + h\vartheta_j)}$ which includes the pondermotive phase and betatron phase detuning. This is different than the analogous FEL equation [1, (3.68)] which has a bunching factor $\sum_{j=1}^{N_e} e^{-i\nu\theta_j}$ that includes only the pondermotive phase. In both cases the radiation power is proportional to the absolute value of this factor squared. If the arguments of the complex exponential are randomly distributed, which is the case for a bunch with no microscopic structure, many of the terms in the sum will cancel each-other out causing the power to scale as $P \propto N_e$. What is physically happening in this case is that the radiation emitted by the particles have random phases and destructively interfere, or in other words the bunch is radiating incoherently. If the bunch instead has microscopic structure such that the complex exponential arguments are all equal (modulo 2π), the terms in the sum add causing the power to scale as $P \propto N_e^2$. In this case, the radiation is emitted with the same phases and adds constructively, or in other words the bunch is radiating coherently.

The difference between $e^{-i(\nu\theta_j + h\vartheta_j)}$ in the ICL equation and the $e^{-i\nu\theta_j}$ in the FEL equation is the mathematical manifestation of a subtle but crucial difference between the ICL and FEL. A bunch in an FEL radiates coherently when $\nu\theta_j \bmod 2\pi$ are all equal, which occurs only when the bunch is microbunched at the radiation wavelength λ . A bunch in an ICL however radiates coherently when $\nu\theta_j + h\vartheta_j \bmod 2\pi$ are all equal which can occur in different ways. The bunch could have $\nu\theta_j \bmod 2\pi$ the same for each particle and $h\vartheta_j \bmod 2\pi$ the same for each particle, in which case it would be microbunched at λ_1 . The bunch could also have a uniform random distribution of both θ_j and ϑ_j but with a correlation between the two such that $\nu\theta_j + h\vartheta_j \bmod 2\pi$ are equal for each particle. This would be bunch with no microbunching “microsnaked” in space at wavelength λ . Bunches with

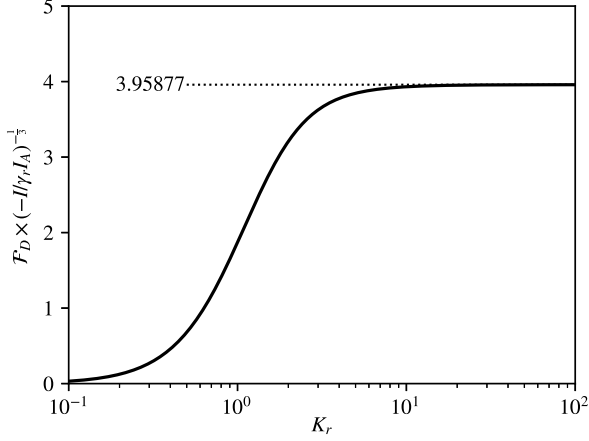


FIG. 1. Dependence of the Fresnel parameter \mathcal{F}_D defined in Eq. (22) on the undulator parameter K_r , assuming $|\Delta\nu| \ll 1$. \mathcal{F}_D quantifies the level of diffraction in an ICL with smaller values corresponding to a greater degree of diffraction. Note that $\mathcal{F}_D \times (-I/\gamma_r I_A)^{-1/3}$ is plotted instead of \mathcal{F}_D directly to pull out the dependence on I and γ_r .

a combination of microbunching and microsaking could also radiate coherently. While we note the complexity of

the microscopic physics of the ICL, a full investigation of it is beyond the scope of this paper.

E. Maxwell-Klimontovich Equations

The period averaged pendulum equations Eq. (13) and field equation Eq. (17) form a system of $4N_e + 1$ equations that describe the physics of the ICL instability. As in FEL theory [1], we can reduce the number of equations to only two by introducing a distribution function and writing down the Maxwell-Klimontovich equations. For the ICL, the distribution function is

$$f(\eta, \delta, \vartheta, \theta, z) = \frac{2\pi}{N_{\lambda_{1,r}}} \sum_{j=1}^{N_e} \delta(\eta - \eta_j(z)) \delta(\delta - \delta_j(z)) \times \delta(\vartheta - \vartheta_j(z)) \delta(\theta - \theta_j(z)) \quad (18)$$

where $N_{\lambda_{1,r}} = |I|\lambda_{1,r}$ is the number of particles in one longitudinal slice of length $\lambda_{1,r}$. We have chosen this normalization arbitrarily. The right hand side of the field equation Eq. (17) can be rewritten as an integral over f and the Klimontovich equation can be computed from $df/dz = 0$ using the pendulum equations Eq. (13). The resulting system of equations is

$$\begin{aligned} & \left[\frac{\partial}{\partial z} + i\Delta\nu k_{\beta,r} - \frac{i}{2\nu k_{1,r}} \nabla_{\perp}^2 \right] \mathcal{A}_h(\mathbf{x}_{\perp}, \nu, z) = -\frac{K_r [\text{JJ}]_h N_{\lambda_{1,r}} \mathcal{W}_h(\mathbf{x}_{\perp})}{4\pi\nu I_A \gamma_r} \iiint\!\!\!\int d\eta d\delta d\vartheta d\theta e^{-i\nu\theta} e^{-ih\vartheta} f(\eta, \delta, \vartheta, \theta, z) \\ & \left[\frac{\partial}{\partial z} + \left[\sum_{h \in \mathbb{N}^+} \int_{\nu \approx h} d\nu \frac{\nu k_{1,r} K_r [\text{JJ}]_h e^{ih\vartheta} e^{i\nu\theta}}{2\gamma_r^2} \int d^2\mathbf{x}_{\perp} \mathcal{W}_h(\mathbf{x}_{\perp}) \mathcal{A}_h(\mathbf{x}_{\perp}, \nu, z) + \text{c.c.} \right] \left(\frac{\partial}{\partial \eta} + \frac{1 + K_r^2}{2K_r^2} \frac{\partial}{\partial \delta} \right) \right. \\ & \left. + 2k_{\beta,r} \left(\eta - \frac{K_r^2}{2 + K_r^2} \delta \right) \frac{\partial}{\partial \theta} - \frac{1}{2} k_{\beta,r} \eta \frac{\partial}{\partial \vartheta} \right] f(\eta, \delta, \vartheta, \theta, z) = 0. \end{aligned} \quad (19)$$

If not explicitly specified, the bounds of ϑ integrals are from 0 to 2π , θ integrals are from 0 to $k_{1,r} L_b$ where L_b is the bunch length, and all other integrals are from $-\infty$ to ∞ . In Appendix D, we verify that Eq. (19) obeys conservation of energy. Introducing normalized quantities, Eq. (19) becomes

$$\begin{aligned} & \left[\frac{\partial}{\partial \hat{z}} + i\Delta\hat{\nu} - i\mathcal{F}_D^{-1} \hat{\nabla}_{\perp}^2 \right] \hat{\mathcal{A}}_h(\hat{\mathbf{x}}_{\perp}, \nu, \hat{z}) = -\frac{1}{2\nu \mathcal{I}} \frac{[\text{JJ}]_h^2}{[\text{JJ}]_1^2} \hat{\mathcal{W}}_h(\hat{\mathbf{x}}_{\perp}) \iiint\!\!\!\int d\hat{\eta} d\hat{\delta} d\hat{\vartheta} d\hat{\theta} e^{-i\nu\hat{\theta}} e^{-ih\hat{\vartheta}} \hat{f}(\hat{\eta}, \hat{\delta}, \hat{\vartheta}, \hat{\theta}, \hat{z}) \\ & \left[\frac{\partial}{\partial \hat{z}} + \hat{\eta}' \left(\frac{\partial}{\partial \hat{\eta}} + \frac{1 + K_r^2}{2K_r^2} \frac{\partial}{\partial \hat{\delta}} \right) + \left(\hat{\eta} - \frac{K_r^2}{2 + K_r^2} \hat{\delta} \right) \frac{\partial}{\partial \hat{\theta}} - \frac{\hat{\eta}}{4} \frac{\partial}{\partial \hat{\vartheta}} \right] \hat{f}(\hat{\eta}, \hat{\delta}, \hat{\vartheta}, \hat{\theta}, \hat{z}) = 0 \end{aligned} \quad (20)$$

where

$$\hat{\eta}' = \sum_{h \in \mathbb{N}^+} \int_{\nu \approx h} d\nu \nu e^{ih\vartheta} e^{i\nu\theta} \int d^2\hat{\mathbf{x}}_{\perp} \hat{\mathcal{W}}_h(\hat{\mathbf{x}}_{\perp}) \hat{\mathcal{A}}_h(\hat{\mathbf{x}}_{\perp}, \nu, \hat{z}) + \text{c.c.} \quad (21)$$

and where we have switched to normalized coordinates $\hat{z} = 2k_{\beta,r} \rho_0 z$, $\hat{\mathbf{x}}_{\perp} = \mathbf{x}_{\perp} / a_{\beta,r}$, $\Delta\hat{\nu} = \Delta\nu / (2\rho_0)$, $\hat{\eta} = \eta / \rho_0$,

$\hat{\delta} = \delta / \rho_0$, $\hat{\mathcal{W}} = \mathcal{W} a_{\beta,r}^2$, $\hat{\mathcal{A}}_h = 2\xi_r [\text{JJ}]_h / (K_r \rho_0^2) \mathcal{A}_h$, $\hat{f} =$

$f\rho_0^2$, and where we have defined the Fresnel parameter

$$\mathcal{F}_D \equiv 4\nu k_{1,r} k_{\beta,r} \rho_0 a_{\beta,r}^2 = 32\nu \xi_r \rho_0, \quad (22)$$

the Cold 1D gain parameter

$$\rho_0 = \left(\frac{|I| \mathcal{I}[\text{JJ}]_1^2}{I_A 8\gamma_r} \right)^{\frac{1}{3}}, \quad (23)$$

and the ‘‘ICL factor’’

$$\mathcal{I} \equiv \frac{4 + K_r^2}{4(2 + K_r^2)}. \quad (24)$$

The interpretation of these three quantities is discussed in the following three paragraphs.

The Fresnel parameter Eq. (22) is defined analogously to Pellegrini *et al.* [2] and quantifies the effect of diffraction in the ICL. It can be written as $\mathcal{F}_D = (4/\sqrt{3})z_R/L_{G,0} \approx 2.3z_R/L_{G,0}$ where $L_{G,0} = \lambda_{\beta,r}/(4\pi\sqrt{3}\rho_0)$ is the Cold 1D gain length, and $z_R = (1/2)\nu k_{1,r} a_{\beta,r}^2$ is the Rayleigh length of a Gaussian mode of waist $a_{\beta,r}$, which is an approximation of the actual radiation waist. The impact of diffraction is greatest when \mathcal{F}_D is smallest. A plot of the dependence of \mathcal{F}_D on K_r is shown in Figure 1. Diffraction is much more significant at lower K_r and plateaus at $K_r \gtrsim 2$. There is little reason to operate an ICL at $K \lesssim 2$. In the on-axis configuration of the ICL [20], the particles’ normalized transverse momenta are assumed to be much less than one, i.e. $K_j \ll 1$. In this case, K_j drops out of Eq. (6) for $\lambda_{1,j}$ and so the spread in K_j due to nonzero emittance cannot induce a spread in $\lambda_{1,j}$ that damps the instability. While this circumvents the stringent emittance requirements of the off-axis ICL, we can see from Figure 1 that it introduces a new problem as the degree of diffraction at $K_j \ll 1$ becomes extremely large, which is what makes the on-axis configuration unfeasible.

The Cold 1D gain parameter is defined in Eq. (23). While this definition was made arbitrarily, we show later on in Section II G that in the 1D limit with no detuning or spread in energy or undulator parameter and for $h = 1$, ρ as defined in terms of the power gain length in Eq. (7) reduces to ρ_0 as defined in Eq. (23). Unlike in the FEL, ρ_0 has no dependence on lasing wavelength or bunch size and only a very weak dependence on K_r (although ρ which unlike ρ_0 includes effects of diffraction becomes very small for $K_r \lesssim 2$ due to the

corresponding increase in diffraction). There is also no dependence of ρ_0 on plasma density. Very high values of ρ_0 can be achieved in the ICL, as compared to the FEL. If we consider, for example, the parameters of the LPA-driven XUV FEL demonstrated in Wang *et al.* [11] ($K = 1.41$, $\gamma m_e c^2 = 490$ MeV, $I = 5.7$ kA, $\sigma_x = 50$ μm , $\sigma_y = 70$ μm , $\lambda_u = 25$ mm), $\rho_{0,\text{ICL}} = 0.023$ while $\rho_{0,\text{FEL}} = 0.0054$. For slightly longer wavelengths where γ is typically low, it could be possible to reach regimes where ρ becomes close enough to unity where the physics of the instability begins to deviate from our theoretical results, which assume $\rho \ll 1$, although this regime is beyond the scope of this paper.

The ICL factor Eq. (24) quantifies some of the subtle differences between the physics of the FEL and the ICL in 1D. If we start with the equation for the 1D FEL gain parameter [1, (3.87)], take $\pi a_{\beta,r}^2$ to be the transverse area, and use the equation $K_r = \gamma_r k_{\beta,r} a_{\beta,r}$ and the resonance condition Eq. (6), we can derive an equation identical to Eq. (23) save for the factor of $\mathcal{I}^{1/3}$. This extra factor arises due to the z evolution of K_j and ϑ_j and the dependence of k_β on energy. It is accounted for when properly deriving the ICL equations, but not when making simple arguments ignoring the differences between FELs and ICLs. \mathcal{I} is order unity for all values of K , with $1/4 \leq \mathcal{I} \leq 1/2$.

The Maxwell-Klimontovich equations in Eq. (20) describe many aspects of the physics of the ICL including the startup process, exponential gain, and saturation. Moving forward, we split the distribution function into a θ -independent background plus a perturbation: $\hat{f}(\hat{\eta}, \hat{\delta}, \vartheta, \theta, \hat{z}) = \hat{f}_0(\hat{\eta}, \hat{\delta}, \vartheta, \theta, \hat{z}) + \hat{f}_1(\hat{\eta}, \hat{\delta}, \vartheta, \theta, \hat{z})$ where the bunch has no microscopic structure at $\hat{z} = 0$, i.e. $\hat{f}_1(\hat{\eta}, \hat{\delta}, \vartheta, \theta, 0) = 0$. Linearizing the Maxwell-Klimontovich equations in this way still allows them to describe the physics of the exponential gain, though they no longer conserve energy or accurately capture the saturation physics.

From Eq. (18) and the definitions for the normalized units, $\int d\hat{\eta} d\hat{\delta} d\vartheta d\theta \hat{f}(\hat{\eta}, \hat{\delta}, \vartheta, \theta, \hat{z}) = 2\pi N_e/N_{\lambda_{1,r}}$. Since the θ integration is performed over an interval $k_1 L_b = 2\pi N_e/N_{\lambda_{1,r}}$, the normalization condition for \hat{f}_0 is

$$\iiint d\hat{\eta} d\hat{\delta} d\vartheta \hat{f}_0(\hat{\eta}, \hat{\delta}, \vartheta, \hat{z}) = 1 \quad (25)$$

where again, the ϑ integral is from 0 to 2π and the other integrals are from $-\infty$ to ∞ .

The linearized Klimontovich equation is

$$\left[\frac{\partial}{\partial \hat{z}} + \left(\hat{\eta} - \frac{K_r^2}{2 + K_r^2} \hat{\delta} \right) \frac{\partial}{\partial \theta} - \frac{\hat{\eta}}{4} \frac{\partial}{\partial \vartheta} \right] \hat{f}_1(\hat{\eta}, \hat{\delta}, \vartheta, \theta, \hat{z}) = - \left[\frac{\partial}{\partial \hat{z}} + \hat{\eta}' \left(\frac{\partial}{\partial \hat{\eta}} + \frac{1 + K_r^2}{2K_r^2} \frac{\partial}{\partial \hat{\delta}} \right) - \frac{\hat{\eta}}{4} \frac{\partial}{\partial \vartheta} \right] \hat{f}_0(\hat{\eta}, \hat{\delta}, \vartheta, \hat{z}) \quad (26)$$

where the higher order \hat{A}_{f_1} term is neglected. We introduce the transformed distribution function

$$\begin{aligned} F(\hat{\eta}, \hat{\delta}, \vartheta, \nu, \hat{z}) &= e^{-ih\vartheta} \int d\theta e^{-i\nu\theta} \hat{f}(\hat{\eta}, \hat{\delta}, \vartheta, \theta, \hat{z}) \\ \hat{f}_1(\hat{\eta}, \hat{\delta}, \vartheta, \theta, \hat{z}) &= \frac{1}{2\pi} \int d\nu e^{i\nu\theta} e^{ih\vartheta} F(\hat{\eta}, \hat{\delta}, \vartheta, \nu, \hat{z}) - \hat{f}_0(\hat{\eta}, \hat{\delta}, \vartheta, \hat{z}) \end{aligned} \quad (27)$$

which allows Eq. (26) to be rewritten as

$$\begin{aligned} \left[\frac{\partial}{\partial \hat{z}} + i\hat{\Delta}\nu - i\mathcal{F}_D^{-1}\hat{\nabla}_{\perp}^2 \right] \hat{\mathcal{A}}_h(\hat{\mathbf{x}}_{\perp}, \nu, \hat{z}) &= -\frac{1}{2\nu\mathcal{I}} \frac{[\text{JJ}]_h^2}{[\text{JJ}]_1^2} \hat{\mathcal{W}}_h(\hat{\mathbf{x}}_{\perp}) \iiint d\hat{\eta} d\hat{\delta} d\vartheta F(\hat{\eta}, \hat{\delta}, \vartheta, \nu, \hat{z}) \\ \left[\frac{\partial}{\partial \hat{z}} + i \left(\left(\nu - \frac{h}{4} \right) \hat{\eta} - \nu \frac{K_r^2}{2 + K_r^2} \hat{\delta} \right) - \frac{\hat{\eta}}{4} \frac{\partial}{\partial \vartheta} \right] F(\hat{\eta}, \hat{\delta}, \vartheta, \nu, \hat{z}) &= \\ -2\pi\nu \left(\frac{\partial \hat{f}_0}{\partial \hat{\eta}} + \frac{1 + K_r^2}{2K_r^2} \frac{\partial \hat{f}_0}{\partial \hat{\delta}} \right) \int d^2 \hat{\mathbf{x}}_{\perp} \hat{\mathcal{W}}_h(\hat{\mathbf{x}}_{\perp}) \hat{\mathcal{A}}_h(\hat{\mathbf{x}}_{\perp}, \nu, \hat{z}). \end{aligned} \quad (28)$$

This can be further simplified by integrating the Klimontovich equation in Eq. (28) with respect to ϑ and using the fact that $F(\hat{\eta}, \hat{\delta}, \vartheta + 2\pi, \nu, \hat{z}) = F(\hat{\eta}, \hat{\delta}, \vartheta, \nu, \hat{z})$ to get

$$\begin{aligned} \left[\frac{\partial}{\partial \hat{z}} + i\hat{\Delta}\nu - i\mathcal{F}_D^{-1}\hat{\nabla}_{\perp}^2 \right] \hat{\mathcal{A}}(\hat{\mathbf{x}}_{\perp}, \nu, \hat{z}) &= -\frac{1}{2\nu\mathcal{I}} \frac{[\text{JJ}]_h^2}{[\text{JJ}]_1^2} \hat{\mathcal{W}}_h(\hat{\mathbf{x}}_{\perp}) \iint d\hat{\eta} d\hat{\delta} \mathcal{F}(\hat{\eta}, \hat{\delta}, \nu, \hat{z}) \\ \left[\frac{\partial}{\partial \hat{z}} + i \left(\left(\nu - \frac{h}{4} \right) \hat{\eta} - \nu \frac{K_r^2}{2 + K_r^2} \hat{\delta} \right) \right] \mathcal{F}(\hat{\eta}, \hat{\delta}, \nu, \hat{z}) &= \\ -2\pi\nu \left(\int d\vartheta \left(\frac{\partial \hat{f}_0}{\partial \hat{\eta}} + \frac{1 + K_r^2}{2K_r^2} \frac{\partial \hat{f}_0}{\partial \hat{\delta}} \right) \right) \int d^2 \hat{\mathbf{x}}_{\perp} \hat{\mathcal{W}}_h(\hat{\mathbf{x}}_{\perp}) \hat{\mathcal{A}}_h(\hat{\mathbf{x}}_{\perp}, \nu, \hat{z}) \end{aligned} \quad (29)$$

where $\mathcal{F}(\hat{\eta}, \hat{\delta}, \nu, \hat{z}) \equiv \int d\vartheta F(\hat{\eta}, \hat{\delta}, \vartheta, \nu, \hat{z})$. These are the linearized Maxwell-Klimontovich equations that describe the growth of the ICL instability. The second equation of Eq. (29) can be integrated to give an expression for $\mathcal{F}(\hat{\eta}, \hat{\delta}, \nu, \hat{z})$, which can be substituted into the first equation to yield the following differo-integral equation describing the \hat{z} -evolution of $\hat{\mathcal{A}}_h$

$$\left[\frac{\partial}{\partial \hat{z}} + i\hat{\Delta}\nu - i\mathcal{F}_D^{-1}\hat{\nabla}_{\perp}^2 \right] \hat{\mathcal{A}}_h(\hat{\mathbf{x}}_{\perp}, \nu, \hat{z}) = \hat{\mathcal{W}}_h(\hat{\mathbf{x}}_{\perp}) \int_0^{\hat{z}} d\hat{z}' \mathcal{X}_h(\hat{z}, \hat{z}') \int d^2 \hat{\mathbf{x}}'_{\perp} \hat{\mathcal{W}}_h(\hat{\mathbf{x}}'_{\perp}) \hat{\mathcal{A}}_h(\hat{\mathbf{x}}'_{\perp}, \nu, \hat{z}') \quad (30)$$

where we have defined

$$\mathcal{X}_h(\hat{z}, \hat{z}') = \frac{\pi}{\mathcal{I}} \frac{[\text{JJ}]_h^2}{[\text{JJ}]_1^2} \iiint d\hat{\eta} d\hat{\delta} d\vartheta e^{-i \left(\left(\nu - \frac{h}{4} \right) \hat{\eta} - \nu \frac{K_r^2}{2 + K_r^2} \hat{\delta} \right) (\hat{z} - \hat{z}')} \times \left[\frac{\partial}{\partial \hat{\eta}} + \frac{1 + K_r^2}{2K_r^2} \frac{\partial}{\partial \hat{\delta}} \right] \hat{f}_0(\hat{\eta}, \hat{\delta}, \vartheta, \hat{z}'). \quad (31)$$

In Appendix E, we compute Eq. (31) for a bunch with both a Gaussian spread and no spread in $\hat{\eta}$ and $\hat{\delta}$. Eq. (30) is the equation for the ICL initial value problem, which is solved numerically in Sections III and IV.

F. Van Kampen Normal Mode Expansion

In this section we follow existing 3D FEL theory by applying a Van Kampen normal mode expansion [1, 44] to solve the initial value problem of Eq. (29). For this subsection only we let the dependence of quantities on ν , h , $\hat{\eta}$, $\hat{\delta}$, and $\hat{\mathbf{x}}_{\perp}$ be implicit in our notation. Further, in this section we assume \hat{f}_0 is independent of \hat{z} . Additionally

we define

$$\begin{aligned} \mathcal{D} &\equiv \hat{\Delta}\nu - \mathcal{F}_D^{-1}\hat{\nabla}_{\perp}^2 \\ \mathcal{G} &\equiv \int d\vartheta \left(\frac{\partial \hat{f}_0}{\partial \hat{\eta}} + \frac{1 + K_r^2}{2K_r^2} \frac{\partial \hat{f}_0}{\partial \hat{\delta}} \right) \\ \Xi &\equiv \left(\nu - \frac{h}{4} \right) \hat{\eta} - \nu \frac{K_r^2}{2 + K_r^2} \hat{\delta} \\ R_J &\equiv \frac{[\text{JJ}]_h^2}{[\text{JJ}]_1^2} \end{aligned} \quad (32)$$

which will simplify notation moving forward. We define

a Hilbert space with state vectors $\Psi(\hat{z}) \equiv (\hat{\mathcal{A}}(\hat{z}) \ \mathcal{F}(\hat{z}))^\top$ and inner product

$$\langle \Psi_1, \Psi_2 \rangle \equiv \int d^2 \hat{\mathbf{x}}_\perp \hat{\mathcal{A}}_1 \hat{\mathcal{A}}_2 + \int d\hat{\eta} d\hat{\delta} \mathcal{F}_1 \mathcal{F}_2. \quad (33)$$

On this space, we define the linear operator \mathcal{M} by its action on an arbitrary state vector $\Psi(\hat{z})$:

$$\mathcal{M}\Psi(\hat{z}) \equiv \begin{pmatrix} \hat{\mathcal{D}}\hat{\mathcal{A}}(\hat{z}) - \frac{iR_J}{2\nu\mathcal{I}}\hat{\mathcal{W}} \int d\hat{\eta} d\hat{\delta} \mathcal{F}(\hat{z}) \\ -2\pi i\nu\mathcal{G} \int d^2 \hat{\mathbf{x}}_\perp \hat{\mathcal{W}}\hat{\mathcal{A}}(\hat{z}) + \Xi\mathcal{F}(\hat{z}) \end{pmatrix}. \quad (34)$$

We have chosen \mathcal{M} so that Eq. (29) is equivalent to

$$i\frac{\partial}{\partial \hat{z}}\Psi(\hat{z}) = \mathcal{M}\Psi(\hat{z}) \quad (35)$$

which is of the same form as the Schrödinger equation. Unlike the Hamiltonian operator in the Schrödinger equation however, \mathcal{M} is not necessarily Hermitian. The action of \mathcal{M}^\dagger on a state vector can be computed using the definition of the Hermitian conjugate $\langle \Psi_1, \mathcal{M}\Psi_2 \rangle = \langle \mathcal{M}^\dagger\Psi_1, \Psi_2 \rangle$ and Eq. (33), which together yield

$$\mathcal{M}^\dagger\Psi(\hat{z}) \equiv \begin{pmatrix} \hat{\mathcal{D}}\hat{\mathcal{A}}(\hat{z}) - 2\pi i\nu R_J \hat{\mathcal{W}} \int d\hat{\eta} d\hat{\delta} \hat{\mathcal{G}}\mathcal{F}(\hat{z}) \\ -\frac{i}{2\nu\mathcal{I}} \int d^2 \hat{\mathbf{x}}_\perp \hat{\mathcal{W}}\hat{\mathcal{A}}(\hat{z}) + \Xi\mathcal{F}(\hat{z}) \end{pmatrix}. \quad (36)$$

We now introduce the normal modes $\Psi_\ell(\hat{z})$, which are solutions to Eq. (35) of the form $\Psi_\ell(\hat{z}) = e^{-i\mu_\ell \hat{z}}\Psi_\ell$, where $\Psi_\ell = (\hat{\mathcal{A}}_\ell \ \mathcal{F}_\ell)^\top$ is independent of \hat{z} . Eq. (35) is now simply the eigenvalue equation $\mathcal{M}\Psi_\ell = \mu_\ell\Psi_\ell$. We define Ψ_ℓ^\dagger and μ_ℓ^\dagger through the adjoint eigenvalue equation $\mathcal{M}^\dagger\Psi_\ell^\dagger = \mu_\ell^\dagger\Psi_\ell^\dagger$. Writing out the two eigenvalue equations for each of the two vector components gives four equations, two of which can be solved to give

$$\begin{aligned} \mathcal{F}_\ell &= -2\pi i\nu \frac{\mathcal{G}}{\mu_\ell - \Xi} \int d^2 \hat{\mathbf{x}}_\perp \hat{\mathcal{W}}\hat{\mathcal{A}}_\ell \\ \mathcal{F}_\ell^\dagger &= -\frac{i}{2\nu\mathcal{I}} \frac{1}{\mu_\ell^\dagger - \Xi} \int d^2 \hat{\mathbf{x}}_\perp \hat{\mathcal{W}}\hat{\mathcal{A}}_\ell^\dagger \end{aligned} \quad (37)$$

which can be substituted into the other two equations to get the dispersion relations for $\hat{\mathcal{A}}_\ell$ and $\hat{\mathcal{A}}_\ell^\dagger$:

$$\begin{aligned} [\mu_\ell - \hat{\mathcal{D}}] \hat{\mathcal{A}}_\ell - \pi\mathcal{V}(\mu_\ell)\hat{\mathcal{W}} \int d^2 \mathbf{x}_\perp \hat{\mathcal{W}}\hat{\mathcal{A}}_\ell &= 0 \\ [\mu_\ell^\dagger - \hat{\mathcal{D}}] \hat{\mathcal{A}}_\ell^\dagger - \pi\mathcal{V}(\mu_\ell^\dagger)\hat{\mathcal{W}} \int d^2 \mathbf{x}_\perp \hat{\mathcal{W}}\hat{\mathcal{A}}_\ell^\dagger &= 0 \end{aligned} \quad (38)$$

where

$$\mathcal{V}(\mu) \equiv -\frac{R_J}{\mathcal{I}} \iint d\hat{\eta} d\hat{\delta} \frac{\mathcal{G}}{\mu - \Xi}. \quad (39)$$

Since the two dispersion relations are identical, we can set $\hat{\mathcal{A}}_\ell^\dagger = \hat{\mathcal{A}}_\ell$ and $\mu_\ell^\dagger = \mu_\ell$. As in FEL Theory [45], we assume the set of eigenvectors $\{\Psi_\ell\}$ are complete and the eigenvalues μ_ℓ are not degenerate. From non-degeneracy,

$$\begin{aligned} 0 &= \langle \Psi_\ell^\dagger, \mathcal{M}\Psi_m \rangle - \langle \mathcal{M}^\dagger\Psi_\ell^\dagger, \Psi_m \rangle \\ &= \langle \Psi_\ell^\dagger, \mu_m \Psi_m \rangle - \langle \mu_\ell^\dagger \Psi_\ell^\dagger, \Psi_m \rangle \\ &= (\mu_m - \mu_\ell) \langle \Psi_\ell^\dagger, \Psi_m \rangle \\ &\implies \langle \Psi_\ell^\dagger, \Psi_m \rangle = \delta_{\ell,m} \langle \Psi_\ell^\dagger, \Psi_m \rangle. \end{aligned} \quad (40)$$

which, along with completeness, allows us to write down the general solution to the initial value problem

$$\Psi(\hat{z}) = \sum_\ell \frac{\langle \Psi_\ell^\dagger, \Psi(0) \rangle}{\langle \Psi_\ell^\dagger, \Psi_\ell \rangle} \Psi_\ell e^{-i\mu_\ell \hat{z}}. \quad (41)$$

To use this equation, one would solve the first dispersion relation in Eq. (38) for $\{\hat{\mathcal{A}}_\ell\}$ and $\{\mu_\ell\}$. From these, $\{\mathcal{F}_\ell\}$ and $\{\mathcal{F}_\ell^\dagger\}$ can then be obtained from Eq. (37), noting that $\hat{\mathcal{A}}_\ell^\dagger = \hat{\mathcal{A}}_\ell$. Next, the sets of vectors $\{\Psi_\ell\}$ and $\{\Psi_\ell^\dagger\}$ can be constructed, and using the inner product Eq. (33) and $\Psi(0) = (\hat{\mathcal{A}}(0) \ \mathcal{F}(0))^\top$, Eq. (41) can be used to compute $\Psi(\hat{z}) = (\hat{\mathcal{A}}(\hat{z}) \ \mathcal{F}(\hat{z}))^\top$, which is the solution to the initial value problem of Eq. (29).

G. Dispersion Relation

In the previous section we obtained Eq. (41) which gives the general solution to the initial value problem of the linearized Maxwell-Klimontovich equations in Eq. (29) describing the ICL instability. In practice, however, the main quantities of interest for calculation are the complex growth rate μ_m and transverse radiation mode profile $\hat{\mathcal{A}}_m(\mathbf{x}_\perp)$ of the fastest growing mode. To compute this, one first finds the set of solution pairs $\{(\mu_\ell, \hat{\mathcal{A}}_\ell(\mathbf{x}_\perp))\}$ indexed by ℓ to the dispersion relation Eq. (38), which written out is

$$\begin{aligned} [\mu_\ell - \Delta\hat{\nu} + \mathcal{F}_D^{-1}\hat{\nabla}_\perp^2] \hat{\mathcal{A}}_\ell(\hat{\mathbf{x}}_\perp) \\ - \pi\mathcal{V}(\mu_\ell)\hat{\mathcal{W}}(\hat{\mathbf{x}}_\perp) \int d^2 \hat{\mathbf{x}}'_\perp \hat{\mathcal{W}}(\hat{\mathbf{x}}'_\perp) \hat{\mathcal{A}}_\ell(\hat{\mathbf{x}}'_\perp) &= 0. \end{aligned} \quad (42)$$

The function $\mathcal{V}(\mu)$ appearing in the above is defined in Eq. (39); Using the definitions in Eq. (32) and integrating by parts, it can be rewritten as

$$\begin{aligned} \mathcal{V}(\mu) &= \left(h + \frac{2(3 + K_r^2)}{4 + K_r^2} \Delta\nu \right) \frac{[\text{JJ}]_h^2}{[\text{JJ}]_1^2} \iint \int d\hat{\eta} d\hat{\delta} d\vartheta \\ &\quad \frac{\hat{f}_0(\hat{\eta}, \hat{\delta}, \vartheta)}{\left(\mu - \left(\frac{3}{4}h + \Delta\nu \right) \hat{\eta} + (h + \Delta\nu) \frac{K_r^2}{2 + K_r^2} \hat{\delta} \right)^2}. \end{aligned} \quad (43)$$

In Appendix E, we compute $\mathcal{V}(\mu)$ for bunches with Gaussian spread in $\hat{\eta}$ and $\hat{\delta}$ and a bunch with no spread in these quantities. We denote the solution pair with the complex growth rate that has the largest imaginary part by the subscript m . At large enough \hat{z} , this solution pair becomes the dominant term in the series Eq. (41) and $\hat{\mathcal{A}}(\hat{\mathbf{x}}_\perp, \hat{z}) \propto \hat{\mathcal{A}}_m(\hat{\mathbf{x}}_\perp) e^{-i\mu_m \hat{z}}$. The 3D gain parameter is defined through the equation for the power gain length and is, in terms of the complex growth rate,

$$\rho = \rho_0 \frac{2}{\sqrt{3}} \text{im}(\mu_m). \quad (44)$$

The 1D limit of the theory can be taken by assuming $\hat{\mathcal{A}}_\ell$ has no transverse dependence and then integrating

Eq. (42) over a transverse circle of radius $a_{\beta,r}$. The resulting dispersion relation is $\mu_\ell - \hat{\Delta}\nu - \mathcal{V}(\mu_\ell) = 0$. For a cold bunch with no wavelength detuning and $h = 1$, the dispersion relation reduces to $\mu_\ell^3 = 1$, and from this the growth rate can be shown to satisfy $\rho = \rho_0$. This result agrees with Davoine *et al.* [34], although there is a factor of \mathcal{I} difference between the definition of ρ here and in [34].

III. NUMERICAL ALGORITHM

In order to obtain useful results from the theory presented in Section II, a method to compute gain lengths and transverse radiation profiles from Eqs. (30) or (42) is needed. Like in FEL theory, there are a number of possibilities to approaching this problem. One is the variational principle [1, 46, 47], in which a functional is constructed from the dispersion relation and the transverse radiation profile is approximated by a trial family of functions. Approximate complex growth rates and radiation profiles are obtained by varying the trial function's parameters to minimize the functional. While relatively quick to compute, this method is only an approximation, and while a Gaussian trial function is a good approximation for the radially symmetric fundamental mode of the

FEL, a more complicated trial function is potentially required for the ICL which has an asymmetric source term $\hat{\mathcal{W}}(\hat{\mathbf{x}}_\perp)$ and therefore an asymmetric radiation profile.

Matrix methods [1, 47] are another approach. In [1, 47], the FEL dispersion relation is converted to radial coordinates and Hankel transformed. The resulting equation is discretized over a 1D radial spatial frequency grid yielding a matrix equation which is solved iteratively. While this method could be adapted to the ICL, the radial non-uniformity of $\hat{\mathcal{W}}(\hat{\mathbf{x}}_\perp)$ in Eq. (42) means that a 2D Fourier transform rather than a Hankel transform would be required, and the transformed equation would be discretized over a 2D—rather than 1D—grid of spatial frequencies. This implies that significantly larger matrices would be required for the ICL as compared to the FEL when using the matrix method, drastically increasing the computational cost.

While other more complicated approaches exist such as that of Baxevanis *et al.* [48], rather than attempt to adapt these to the ICL we chose to use a novel, albeit relatively simple, Crank-Nicholson finite difference approach to efficiently solve the ICL initial value problem Eq. (30). The method works as follows. First, we introduce $\mathcal{B}(\hat{\mathbf{x}}_\perp, \hat{z}) \equiv e^{i\hat{\Delta}\nu\hat{z}} \hat{\mathcal{A}}(\hat{\mathbf{x}}_\perp, \nu, \hat{z})$ and $\Gamma(\hat{z}, \hat{z}') \equiv e^{i\hat{\Delta}\nu(\hat{z}-\hat{z}')} \mathcal{X}(\hat{z}, \hat{z}')$, which allows Eq. (30) to be rewritten as

$$\left[\frac{\partial}{\partial \hat{z}} - i\mathcal{F}_D^{-1} \hat{\nabla}_\perp^2 \right] \mathcal{B}(\hat{\mathbf{x}}_\perp, \hat{z}) = \hat{\mathcal{W}}(\hat{\mathbf{x}}_\perp) \int_0^{\hat{z}} d\hat{z}' \Gamma(\hat{z}, \hat{z}') \int d^2 \hat{\mathbf{x}}'_\perp \hat{\mathcal{W}}(\hat{\mathbf{x}}'_\perp) \mathcal{B}(\hat{\mathbf{x}}'_\perp, \hat{z}'). \quad (45)$$

We discretize this equation over a uniform transverse spatial grid. On the left-hand side we discretize using the Crank-Nicholson method in order to ensure numerical stability and speed up the code by allowing larger step sizes. For the source term on the right-hand side we discretize by replacing the integrals with Riemann sums. We use the Euler method (evaluating at \hat{z}) rather than the Crank-Nicholson method (evaluating at \hat{z} and $\hat{z} + d\hat{z}$ and averaging) for the right-hand side as the difference between the two is negligible and the former is simpler. The discretized equation is

$$\begin{aligned} & \frac{\mathcal{B}_{i,j}^{n+1} - \mathcal{B}_{i,j}^n}{d\hat{z}} - \frac{i\mathcal{F}_D^{-1}}{2} \left[\frac{1}{d\hat{x}^2} (\mathcal{B}_{i-1,j}^n - 2\mathcal{B}_{i,j}^n + \mathcal{B}_{i+1,j}^n + \mathcal{B}_{i-1,j}^{n+1} - 2\mathcal{B}_{i,j}^{n+1} + \mathcal{B}_{i+1,j}^{n+1}) \right. \\ & \left. + \frac{1}{d\hat{y}^2} (\mathcal{B}_{i,j-1}^n - 2\mathcal{B}_{i,j}^n + \mathcal{B}_{i,j+1}^n + \mathcal{B}_{i,j-1}^{n+1} - 2\mathcal{B}_{i,j}^{n+1} + \mathcal{B}_{i,j+1}^{n+1}) \right] = \hat{\mathcal{W}}_{i,j} d\hat{z} \sum_{m=0}^{n-1} \Gamma^{n,m} d\hat{x} d\hat{y} \sum_{p,q} \hat{\mathcal{W}}_{p,q} \mathcal{B}_{p,q}^m \end{aligned} \quad (46)$$

where $\mathcal{B}_{i,j}^n = \mathcal{B}(\hat{x}_i, \hat{y}_j, \hat{z}_n)$ and $\Gamma^{n,m} = \Gamma(\hat{z}_n, \hat{z}_m)$, and where in order to discretize $\hat{\mathcal{W}}(\hat{x}, \hat{y})$ we approximated the delta function in Eq. (A7) with a step function centered at $\hat{y} = 0$ of width $d\hat{y}$ and height $1/d\hat{y}$: $\hat{\mathcal{W}}_{i,j} = \hat{\mathcal{W}}_{x,i} \delta_{j,j_0}/d\hat{y} = \hat{\mathcal{W}}_x(\hat{x}_i) \delta_{j,j_0}/d\hat{y}$ where $\hat{\mathcal{W}}_x(\hat{x}) = \int d\hat{y} \hat{\mathcal{W}}(\hat{x}, \hat{y})$ and j_0 is the index where $\hat{y}_{j_0} = 0$. Eq. (46) can be rearranged and converted to the matrix equation

$$\begin{aligned} & (1 - i\mu_x \Delta_x - i\mu_y \Delta_y) \mathcal{B}^{n+1} \\ & = (1 + i\mu_x \Delta_x + i\mu_y \Delta_y) \mathcal{B}^n + \mathcal{C}^n \end{aligned} \quad (47)$$

where

$$\begin{aligned} (\Delta_x)_{i,j,i',j'} & \equiv (\delta_{i-1,i'} - 2\delta_{i,i'} + \delta_{i+1,i'}) \delta_{j,j'} \\ (\Delta_y)_{i,j,i',j'} & \equiv \delta_{i,i'} (\delta_{j-1,j'} - 2\delta_{j,j'} + \delta_{j+1,j'}) \\ (\mathcal{C}^n)_{i,j} & \equiv \delta_{j,j_0} \hat{\mathcal{W}}_{x,i} \frac{d\hat{z}^2 d\hat{x}}{d\hat{y}} \sum_{m=0}^{n-1} \Gamma^{n,m} \left(\sum_p \hat{\mathcal{W}}_{x,p} \mathcal{B}_{p,j_0}^m \right) \\ \mu_x & = d\hat{z}/(2\mathcal{F}_D d\hat{x}^2) \\ \mu_y & = d\hat{z}/(2\mathcal{F}_D d\hat{y}^2). \end{aligned} \quad (48)$$

and where vectors and matrices are constructed by flattening the 2D transverse position indices into 1D using an ordering scheme such as column major (e.g. $\mathcal{B}^n = (B_{11}^n \ B_{21}^n \ \dots \ B_{12}^n \ B_{22}^n \ \dots)^T$) or row major (e.g. $\mathcal{B}^n = (B_{11}^n \ B_{12}^n \ \dots \ B_{21}^n \ B_{22}^n \ \dots)^T$). We note that \mathcal{C}^n depends on the time history $\mathcal{B}^0, \mathcal{B}^1, \dots, \mathcal{B}^{n-1}$.

Due to the large number of grid points and thus dimension of the vectors and matrices involved, it is inefficient to directly solve Eq. (47) numerically every step. Were this in one transverse dimension, the matrices in this equation would be tridiagonal enabling it to be solved using fast and space efficient tridiagonal matrix algorithms. However, in two dimensions this is not the case. If column major ordering is used, Δ_x is tridiagonal but Δ_y is not, and vice-versa for row major ordering. To circumvent this we use the alternating direction implicit method [49], which works by instead solving the approximate equation

$$\begin{aligned} & (1 - i\mu_x \Delta_x)(1 - i\mu_y \Delta_y) \mathcal{B}^{n+1} \\ & = (1 + i\mu_x \Delta_x)(1 + i\mu_y \Delta_y) \mathcal{B}^n \\ & + (1 + i\mu_x \Delta_x)(1 - i\mu_x \Delta_x) \mathcal{C}^n \end{aligned} \quad (49)$$

which is equal to Eq. (47) to first order in μ_x and μ_y which are small, and differs only in the second order terms. Eq. (49) can be broken into two simpler equations by introducing a new vector \mathcal{B}^* which is solved for as an intermediate step:

$$\begin{aligned} (1 - i\mu_x \Delta_x) \mathcal{B}^* & = (1 + i\mu_y \Delta_y) \mathcal{B}^n \\ (1 - i\mu_y \Delta_y) \mathcal{B}^{n+1} & = (1 + i\mu_x \Delta_x)(\mathcal{B}^* + \mathcal{C}^n). \end{aligned} \quad (50)$$

Unlike Eq. (47), it is possible to solve Eq. (50) entirely using tridiagonal algorithms and vastly speed up the computation. This requires reordering the entries of

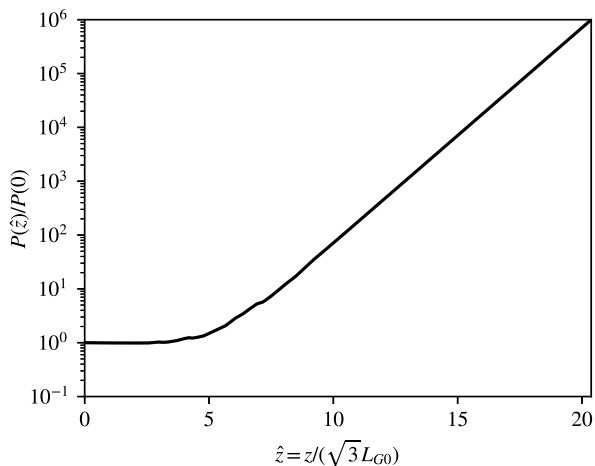


FIG. 2. Simulated radiation power gain of an ICL with the “base” parameters described in Section IV.

vectors to switch between row-major and column-major at various points during the computation.

While in principle this algorithm can be applied to the FEL, in practice it is likely significantly less efficient for the FEL than for the ICL. This is due to different definitions of \mathcal{C}^n which arise from the source term on the right hand side of the \hat{z} -evolution equation (Eq. (30) for the ICL and [48, (18)] for the FEL). In the case of the FEL, to calculate \mathcal{C}^n at each step, a 3D numerical integration over \mathbf{x}'_{\perp} and $z' < z$ must be performed for each transverse grid point \mathbf{x}_{\perp} . In the case of the ICL, due to separability of the integral kernel in Eq. (30) and the fact that $\hat{W}(\hat{x}, \hat{y}) = 0$ when $\hat{y} \neq 0$, only two 1D numerical integrations are needed per step. The first is computing $a_n \equiv \sum_p \hat{W}_{x,p} \mathcal{B}_{p,j_0}^n$ which is added to a list $\{a_0, a_1, \dots, a_{n-1}\}$ which can be stored in memory. The second is computing $\sum_{m=0}^{n-1} \Gamma^{n,m} a_m$. This significant added computational complexity in the FEL case explains why other previously mentioned approaches such as the variational principle or matrix methods are used for FELs instead of the algorithm outlined here.

We developed a Python code implementing the algorithm described in this section. This code computes the \hat{z} -evolution of the transverse radiation profile as well as L_G and ρ by fitting the total radiation power growth to an exponential. For simplicity, we use a square transverse grid with square transverse cells so $\hat{x}_{\max} = \hat{y}_{\max} = -\hat{x}_{\min} = -\hat{y}_{\min}$, $d\hat{x} = d\hat{y}$, and $\mu = \mu_x = \mu_y$. A Gaussian initial radiation field is used to seed the interaction. Convergence of the simulation with respect to transverse box size, transverse cell size, and μ as well as insensitivity of the simulation to the initial radiation shape are demonstrated in Appendix F. This code can simulate both a cold bunch as well as a bunch with Gaussian spread in energy or undulator parameter, and can be run with nonzero frequency detuning $\Delta\nu$.

IV. NUMERICAL RESULTS

Having introduced in the previous section an algorithm to solve the ICL initial value problem Eq. (30), we turn to using it to examine the behavior of the ICL in a number of different cases. First we ran a “base” simulation with parameters $h = 1$, $K_r \rightarrow \infty$, $\hat{\Delta}\nu = 0$, $\Sigma = 0$, and $\rho_0 = 0.01$. The non-physical parameters $\hat{x}_{\max} = 20$, $d\hat{x} = 0.2$, $\mu = 0.5$, and $\sigma_{\hat{x},\text{initial}} = \sigma_{\hat{y},\text{initial}} = 1$ were selected based on convergence scans performed in Appendix F. The simulation showed exponential growth in the radiation power after an initial startup period which can be seen in Figure 2. The evolution of the radiation profile from the initial bi-Gaussian distribution used to seed the interaction to a steady state during this exponential growth regime is shown in Figure 3. The steady state transverse radiation profile is asymmetric near the axis: dropping off faster in \hat{y} than in \hat{x} . However at $\hat{r} \gtrsim 1$ this asymmetry quickly disappears and the field becomes symmetric. This shape is due to the competing

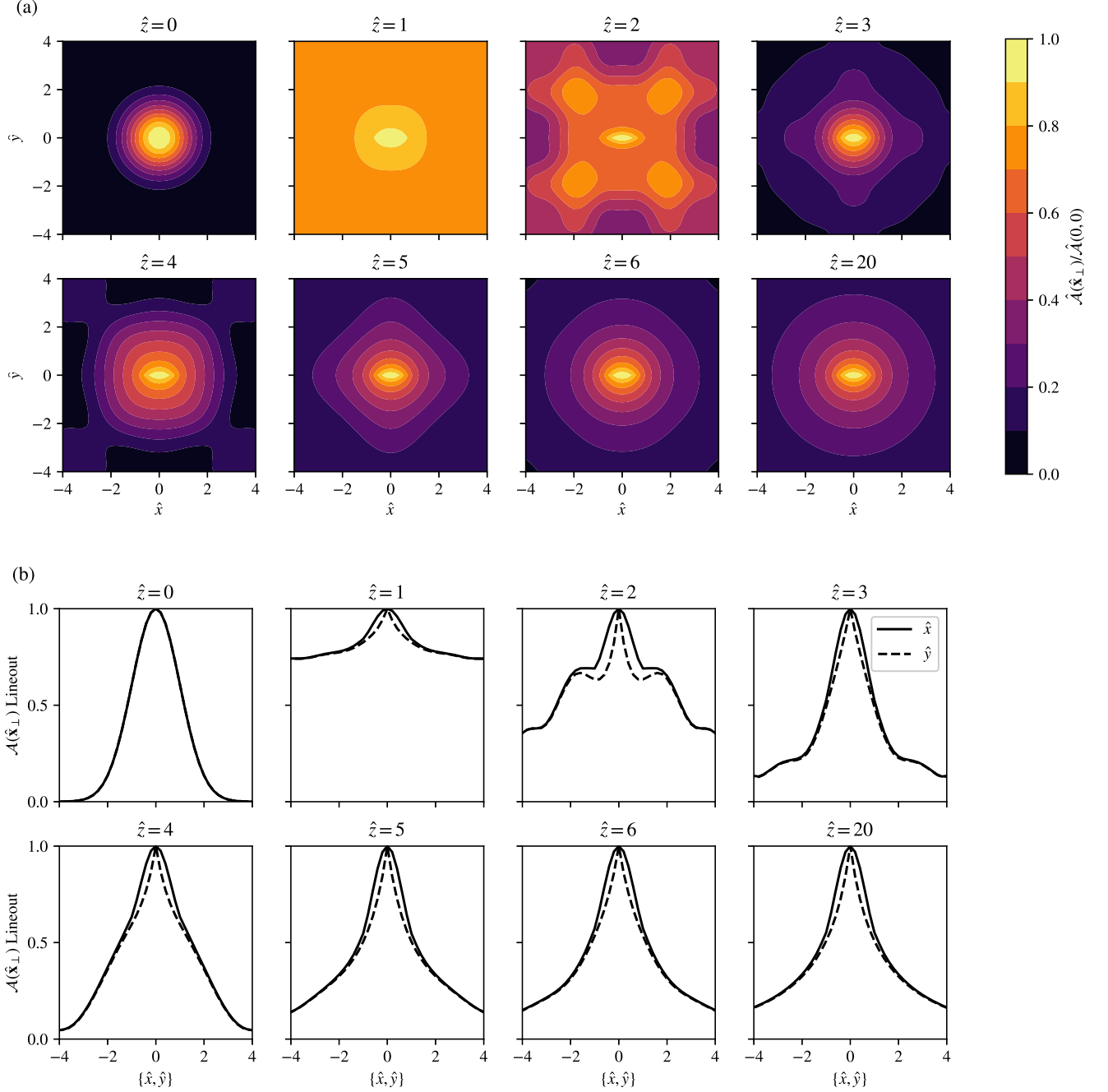


FIG. 3. Simulated transverse radiation profiles at different \hat{z} positions for an ICL with the “base” parameters described in Section IV. (a) Normalized two-dimensional field profile (b) Lineouts at $\hat{y} = 0$ (solid) and $\hat{x} = 0$ (dashed). Figures show the evolution of the radiation profile from the initial seed, through the startup process, to the final steady state.

effects of the asymmetric source term in Eq. (30) and the effect of diffraction due to which higher order (asymmetric) modes diffract faster. In Appendix F we demonstrate that as expected the ICL radiation power growth rate is insensitive to the size of the initial seed radiation field.

We now consider variations to this base case. The dependence of the gain parameter and the (steady state)

transverse radiation sizes on K_r and ρ_0 are shown in Figure 4. Previously, in Section II E we introduced the Fresnel parameter \mathcal{F}_D defined in Eq. (22) which quantifies diffraction. The results in Figure 4 agree with what would be expected from that discussion: for larger ρ_0 and K_r , \mathcal{F}_D is larger, meaning diffraction is less severe and ρ/ρ_0 is larger; for smaller ρ_0 and K_r , \mathcal{F}_D is smaller,

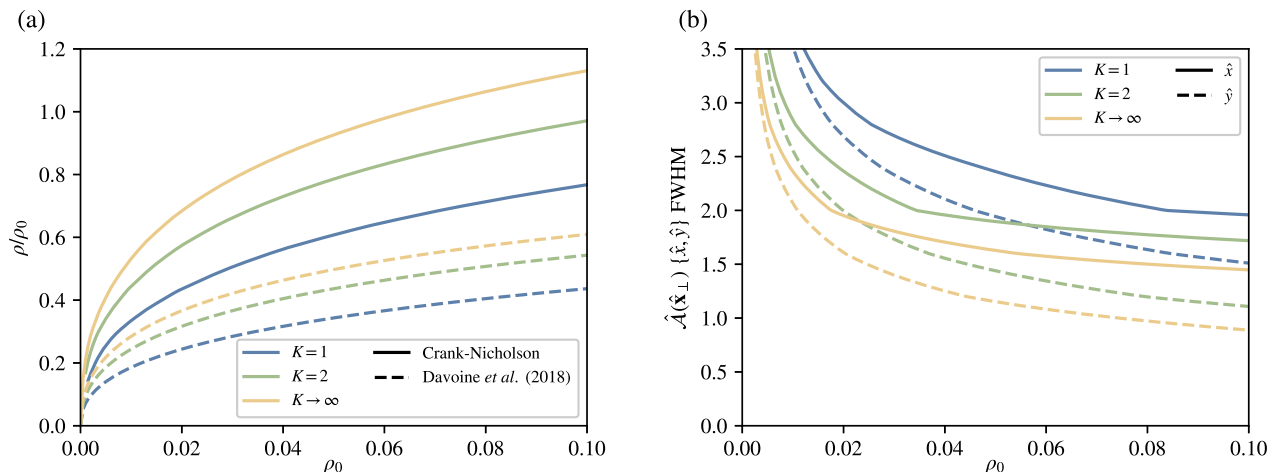


FIG. 4. Dependence of the relative 3D gain parameter (a) and the transverse radiation sizes in \hat{x} (solid lines) and \hat{y} (dashed lines) (b) on the Cold 1D gain parameter ρ_0 for various values of the undulator parameter: $K_r = 1$ (blue), $K_r = 2$ (green), and $K_r \rightarrow \infty$ (yellow). Results are shown for a cold electron bunch with no frequency detuning ($\Delta\nu = 0$) and are computed using the algorithm described in Section III, except for the dashed lines in figure (a) which are computed using the method from Davoine *et al.* [34].

meaning diffraction is more severe and ρ/ρ_0 is smaller. Since $\mathcal{F}_D \propto K_r^2/(2(2 + K_r^2))$, the ability of larger K_r to reduce diffraction plateaus for $K_r \gg 1$.

From Figure 4, we also see the radiation field is smaller and more asymmetric when diffraction is less significant, and larger and more symmetric when diffraction is more significant. Additionally, in this figure we compare the ρ predicted by our theory to that predicted by the theory in [34]. We find [34] gives radiation power growth rates a factor of few smaller than the method presented in this work. We speculate that this is due the fact that in [34], the transverse size of the radiation was assumed to be equal to that of the emitter, which was well approximated by a Gaussian with $\sigma = \frac{3}{8}a_{\beta,r} = 0.375a_{\beta,r}$, i.e. FWHM $\frac{3}{4}\sqrt{2\ln 2}a_{\beta,r} \approx 0.883a_{\beta,r}$. Contrastingly, our theory predicts a larger radiation field, which would have larger gain due to their longer Rayleigh length and thus lower diffraction.

Next we consider a bunch with a Gaussian spread in energy and undulator parameter. As can be seen mathematically in Eq. (E4), the dependence of the ICL physics in this case on energy spread σ_γ and undulator parameter spread σ_K is exclusively through its dependence on the parameter

$$\Sigma = \frac{1}{\rho_0} \left[\left((h + \Delta\nu) \frac{K_r^2}{2 + K_r^2} \frac{\sigma_K}{K_r} \right)^2 + \left(\left(\frac{3}{4}h + \Delta\nu \right) \frac{\sigma_\gamma}{\gamma_r} \right)^2 \right]^{\frac{1}{2}}. \quad (51)$$

This parameter Σ is essentially quantifying the degree to which σ_K and σ_γ violate the constraints on them re-

quired for lasing [34, (1.1)], although ρ_0 instead of ρ appears in Eq. (51). $\Sigma\rho_0/\rho \lesssim 1/2$ is equivalent to these constraints [34, (1.1)]. In Figure 5 we plot the effect of energy and undulator parameter spread on the ICL by plotting the relative change in gain parameter as a function of $\Sigma\rho_0/\rho(\Sigma = 0)$. We see that ρ decreases as Σ is increased, falling essentially to zero by the point $\Sigma = \rho/\rho_0$. This result is important because it quantifies how ICL gain decreases with large bunch emittance and energy spread near the beam quality requirements. This provides more specificity to these beam quality requirements, which are often stated simply as an approximate inequality such as in Section V.

Finally, we see the ICL detuning curve in Figure 6. This curve appears to have a similar shape to that of the FEL but with a significantly larger width of order 1 in an ICL compared to order ρ in an FEL. This could be related to the fact that $\sigma_\perp \ll a_{\beta,r}$ in an ICL while $\sigma_\perp \gg a_{u,r}$ in an FEL. However, we hesitate to make any firm conclusions, one reason being that the theory presented in this work depends on the assumption $|\Delta\nu| \ll 1$ made during the period averaging procedure. We believe the effect of frequency detuning in the ICL merits further study.

V. PHASE SPACE REQUIREMENTS

Elucidating the beam quality requirements for lasing in the ICL is crucial to judging the feasibility of the concept as a whole. In the ICL, like in the FEL, the spread in resonant wavelengths of particles in each longitudinal slice must obey the condition $\Delta\lambda_1/\lambda_{1,r} \lesssim \rho$ for lasing to occur. As discussed previously in Section II B, while for

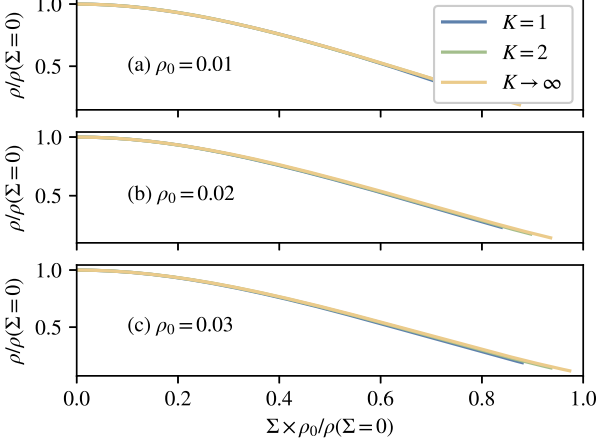


FIG. 5. Effect of finite Gaussian energy/undulator spread on the gain parameter ρ for $K_r = 1$ (blue), $K_r = 2$ (green), and $K_r \rightarrow \infty$ (yellow), and for $\rho_0 = 0.01$ (a), $\rho_0 = 0.02$ (b), and $\rho_0 = 0.03$ (c). Σ is defined in terms of σ_K , σ_γ , and ρ_0 in Eq. (51).

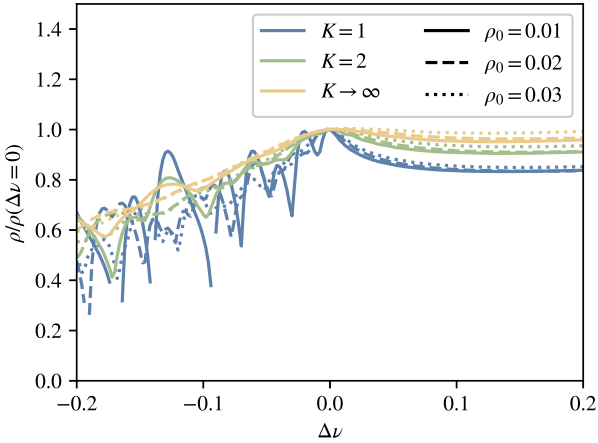


FIG. 6. ICL detuning curve. Proportional change in gain parameter due to nonzero detuning is plotted for different values of $\Delta\nu$. Curves are shown for a range of different parameters: $K_r = 1$ (blue), $K_r = 2$ (green), $K_r \rightarrow \infty$ (yellow), $\rho_0 = 0.01$ (solid), $\rho_0 = 0.02$ (dashed), $\rho_0 = 0.03$ (dotted).

the FEL this implies a constraint on the beam’s angular spread and thus its emittance, differences in the physics mean that for the ICL this condition instead implies a constraint on the beam’s spread in K :

$$\frac{\Delta K}{K} \lesssim \frac{2 + K^2}{2K^2} \rho. \quad (52)$$

While there is no *intrinsic* constraint on the emittance in order to lase in an ICL, for different families of phase space distributions there is a maximum emittance a beam can have for a given ΔK . Along with Eq. (52), this allows a maximum emittance for lasing

to be written down. In this section we derive emittance constraints for three families of phase space distributions: matched offset Gaussian beams, “optimally mismatched” offset Gaussian beams, and “phase space annular sector” beams.

To illustrate these three phase space distribution families and the relationship between K -spread and emittance, consider a bunch in an ion channel containing resonant ($\gamma_j = \gamma_r$), paraxial ($K_j/\gamma_j \ll 1$) electrons oscillating entirely in the $x - z$ plane ($y_j = p_{y,j} = 0$). As discussed in Section II B, the electrons will exhibit simple harmonic betatron motion. In normalized $\gamma k_{\beta x} - p_x$ phase space, they move counterclockwise along circular trajectories of radii K_j . Fig. 7 shows diagrams of each of the three previously mentioned phase space distribution families in this normalized phase space. Fig. 7(a) illustrates how a matched beam, while optimal for the on-axis ICL configuration, demands a relatively small emittance to achieve a given ΔK , making it suboptimal for the off-axis configuration. Note that while matching prevents projected emittance growth due to chromatic phase mixing for an on-axis beam, the same is not true for an off-axis beam, although this projected emittance growth will not cause an increase in ΔK .

As originally pointed out by Ersfeld *et al.* [31], using a mismatched bunch distribution makes it possible to achieve the same ΔK with a larger emittance. This can be seen in Fig. 7(b), which shows an “optimally mismatched” offset Gaussian phase space distribution with spot size and angular spread maximize emittance for a given K -spread. Finally, a non-Gaussian “phase space annular sector” distribution is shown in Fig. 7(c). Such a phase space distribution would enable lasing with even larger emittances but would be challenging to prepare. One potential method could be to send an underfocused, on-axis Gaussian beam through a bending magnet with a stronger kick at smaller $|x|$ than at larger $|x|$. This would produce a beam resembling the one shown in Figure 7(c).

We now move on to a quantitative analysis of these three cases. In Appendix G we write the distribution functions for each case and derive the optimal parameters that minimize emittance for a given wavelength spread subject to the resonance condition. For each case we write the emittance of the optimized distribution as a function of wavelength spread and require $\Delta\lambda_1/\lambda_{1,r} \lesssim \rho$ to obtain the emittance constraint. These calculations consider the full 4D transverse phase space, rather than enforcing the restriction $y = p_y = 0$. The emittance constraints are

$$\epsilon_{n,x}, \epsilon_{n,y} \lesssim \frac{\gamma\lambda_1}{\pi} \frac{1 + \frac{K^2}{2}}{K^2} \rho^2 \quad (53)$$

for the matched offset Gaussian bunch,

$$\begin{aligned} \epsilon_{n,x} &\lesssim \frac{\gamma\lambda_1}{\pi} \left(\frac{2}{5}\right)^{\frac{3}{4}} \left(\frac{1 + \frac{K^2}{2}}{K^2}\right)^{\frac{1}{2}} \rho^{\frac{3}{2}} \\ \epsilon_{n,y} &\lesssim \frac{\gamma\lambda_1}{\pi} \sqrt{\frac{2}{5}} \rho \end{aligned} \quad (54)$$

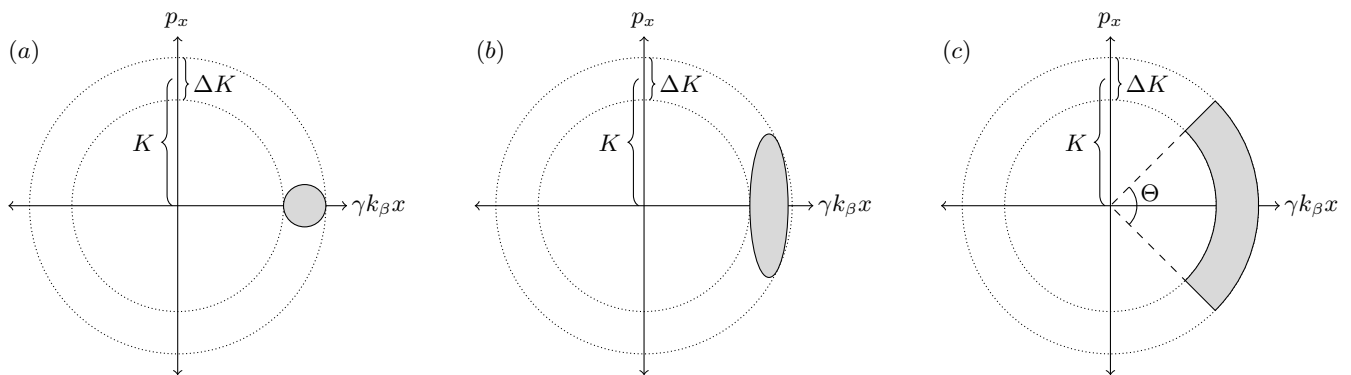


FIG. 7. Conceptual diagram showing (a) matched offset Gaussian, (b) optimally mismatched offset Gaussian, and (c) annular sector bunch distributions shaded in gray in normalized $\gamma k_{\beta x} - p_x$ phase space. Radii of the inner and outer dotted circles give the minimum and maximum tolerable values of K , respectively. Each bunch will rotate clockwise about the origin on a circular path at the betatron frequency. The difference in radii of the dotted circles corresponds to the bunch's K -spread. This figure shows how different bunch phase space distributions can maintain the same spread in K while occupying a larger or smaller volume in phase space, corresponding to a larger or smaller emittance.

for the optimally mismatched offset Gaussian bunch, and

$$\begin{aligned} \epsilon_{n,x} &\lesssim \frac{\gamma \lambda_1}{\pi} \sqrt{6} \rho \\ \epsilon_{n,y} &\lesssim \frac{\gamma \lambda_1}{\pi} \frac{1}{\sqrt{2}} \rho \end{aligned} \quad (55)$$

for the phase space annular sector bunch, where Θ is the total angle subtended by the annular sector in phase space.

As expected, the emittance constraint Eq. (53) on the matched offset Gaussian bunch is the most stringent, followed by the constraint Eq. (54) on the optimally mismatched offset Gaussian bunch and finally by the constraint Eq. (55) on the phase space annular sector bunch which is the least stringent. The emittance constraints in all of these cases are, however, more stringent than those for an FEL [1]

$$\epsilon_{n,x}, \epsilon_{n,y} \lesssim \frac{\gamma \lambda_1}{\pi} \frac{\bar{\beta}}{4L_G} \quad (56)$$

where $\bar{\beta} \approx L_G$ is the beta function.

Before we continue, there is a fourth phase space distribution family that bears mentioning: optimally mismatched, offset Gaussian bunches subject to the constraint $\epsilon_{n,x} = \epsilon_{n,y}$. The emittance constraint in this case is more stringent than Eq. (54) for the optimally mismatched case where $\epsilon_{n,x} \neq \epsilon_{n,y}$, but less stringent than Eq. (53) for the matched case. While we don't include a quantitative analysis of this fourth case due to its analytic complexity, numerically computing the emittance constraint and optimal parameters is relatively straightforward.

There are a number of caveats to the discussion in this section and the emittance constraints Eq. (53)-(55). First, the betatron phases of the phase space distributions shown in Figure 7 and the phase space distribution

functions in Eq. (G1) are arbitrary. These distributions can be rotated in normalized $\gamma k_{\beta x} - p_x$ phase space without changing the emittance constraint. This is important because it may, for instance, be easier to inject a bunch into a plasma with an offset in p_x (an underfocused beam centered in the ion channel but with velocity at an angle with respect to the ion channel axis) than an offset in x (an overfocused beam travelling parallel to but with a transversely displaced centroid position from the axis down the center of the ion channel). Second, we have assumed a monoenergetic bunch in this section. Both K spread due to nonzero emittance and energy spread contribute to the resonant wavelength spread that ultimately damps the instability. A bunch with a correlation between γ and K due to nonzero dispersion could have a lower resonant wavelength spread than one with comparable emittance and no such correlation, and could lase despite exceeding the emittance constraints derived in this section. This is an important point, linear x dispersion can be easily added to a beam with a chicane and could allow these emittance limits to be perhaps significantly exceeded. This is in contrast to beam condition-

TABLE I. Example parameters for an ICL in x-ray and visible wavelengths. Emittance constraints are given by Eq. (54) and are for the optimally mismatched Gaussian bunch case.

λ (nm)	10	400
E (GeV)	3	3
n_0 (cm ⁻³)	10 ¹⁷	10 ¹⁶
I (kA)	20	20
K	10.9	39.0
ρ_0	0.0146	0.0145
ρ	0.00888	0.00882
L_G (cm)	5.92	18.8
$\epsilon_{n,x}$ (nm)	$\lesssim 5.61$	$\lesssim 220$
$\epsilon_{n,y}$ (nm)	$\lesssim 105$	$\lesssim 4170$

ing methods for FELs which are more complicated [50]. Third, the emittance constraints Eq. (53)-(55) are not binary: as these limits are approached, ρ decreases gradually. This was discussed in Section IV with the gradual fall-off computed numerically and shown in Figure 5, although it bears mentioning that the bunch distributions in this section do not have Gaussian K distributions as assumed in Section IV and so these curves are only approximately applicable in this section.

VI. DISCUSSION

We have presented the most complete theory of the ICL to date, accounting for 3D effects, diffraction, transverse radiation shape, frequency and betatron phase detuning, and nonzero emittance and energy spread. Additionally, we have developed a novel numerical algorithm for solving the ICL equations which we have used to compute results for a range of different parameters. Finally, we have discussed in detail the nature of the ICL's beam quality requirements, deriving emittance constraints and the optimal Gaussian beam distribution for lasing in an ICL.

At the same time, there are many topics we have left to future work. We focused on the planar off-axis configuration of the ICL, leaving out discussion of circular and elliptical configurations. Longitudinal spacecharge effects which are important in some regimes are ignored in our theory. While we discuss the microscopic physics and the effect of detuning on ICL performance, we believe both these topics warrant further investigation. What we believe to be the most pressing topic for future research however is running 3D PIC simulations of physical ICL configurations.

Compared to the FEL, the ICL trades a less stringent energy spread constraint for a more stringent emittance constraint. In Section V we showed how the right transverse phase space distribution can relax these constraints somewhat for asymmetric bunches. These constraints could be relaxed further by using a bunch with a linear x dispersion, although we did not examine this case in detail. Hypothetical parameters of an x-ray and visible light ICL are shown in Table I. Achieving such extreme parameters almost certainly would require a bunch from a plasma injector. Plasma injectors are an active area of research, with multiple plasma injection schemes demonstrating in PIC simulations the ability to inject order kA peak current bunches with emittances of order 10nm [51–56]. We speculate that with a plasma source that transitions from a wide radius to a narrow radius, an off-axis plasma injected bunch could lase in an ICL without ever having to outcouple from the plasma.

A proof of principle experiment [35] is planned in the near term at the Facility for Advanced Accelerator Experimental Tests II (FACET-II) [57, 58] at SLAC National Accelerator Laboratory.

ACKNOWLEDGMENTS

We graciously thank Joanna Morgan (LLNL) for assistance running simulations.

This work is supported by the National Science Foundation under grant NSF-2047083 and the US Department of Energy under grant DE-SC0017906.

This research used resources of the National Energy Research Scientific Computing Center (NERSC), a Department of Energy User Facility (project m306-2024).

Appendix A: Period Averaging

In this Appendix we define the period average and derive Eq. (A6) which gives the an expression for a useful period averaged expression which appears in both the pendulum and field equations. During the course of this derivation we define a new function $\mathcal{W}_h(\mathbf{x}_\perp)$ which we plot and discuss the properties of.

For some function $f(z)$, the period average is defined as the average of the quantity over one betatron period

$$\overline{f(z)} \equiv \frac{1}{\lambda_{\beta,r}} \int_{z - \frac{\lambda_{\beta,r}}{2}}^{z + \frac{\lambda_{\beta,r}}{2}} dz f(z). \quad (\text{A1})$$

We make heavy use of the fact that if a function $g(z)$ is slowly varying over one betatron period ($g'(z) \ll k_{\beta,r}g(z)$), then for any $h(z)$, $\overline{g(z)h(z)} \simeq g(z)\overline{h(z)}$.

We begin the derivation of Eq. (A6) by noting a number of identities. First we note that $\forall n \in \mathbb{Z}$,

$$\overline{e^{ink_{\beta,r}z}} = \delta_{n,0} \quad (\text{A2})$$

which can be shown by directly computing the integral in Eq. (A1). Second we note two Jacobi-Anger identities

$$\begin{aligned} e^{ix \sin(\phi)} &= \sum_{n \in \mathbb{Z}} J_n(x) e^{in\phi} \\ e^{-ix \cos(\phi)} &= \sum_{n \in \mathbb{Z}} (-i)^n J_n(x) e^{\pm in\phi} \end{aligned} \quad (\text{A3})$$

where the second identity is true for both $\pm = +$ and $\pm = -$. Third we note that from Eqs. (5) and (8),

$$\begin{aligned} \nu k_{1,r} \zeta_j &= \nu \theta_j - \Delta \nu k_{\beta,r} z \\ &\quad - h k_{\beta,r} z + \nu \xi_j \sin(2(k_{\beta,r} z + \vartheta_j)) \end{aligned} \quad (\text{A4})$$

where $\xi_j \equiv k_{1,r} K_j^2 / (8\gamma_j^2 k_{\beta,j})$. The reference value of this new quantity is $\xi_r = k_{1,r} K_r^2 / (8\gamma_r^2 k_{\beta,r}) = K_r^2 / (2(2 + K_r^2))$. Using Eqs. (A2)-(A4) as well as the definition Eq. (B1) of the \mathcal{C}_n functions discussed in Appendix B and the integral Eq. (B3), we compute the following (where $l \in \mathbb{Z}$)

$$\begin{aligned}
& \overline{\delta^2(\mathbf{x}_\perp - \mathbf{x}_{\perp,j}) e^{il(k_{\beta,r,z} + \vartheta_j)} e^{\pm i\nu k_{1,r}\zeta_j} e^{\pm i\Delta\nu k_{\beta,r,z}}} \\
&= \overline{\delta(x - a_{\beta,j} \cos(k_{\beta,r,z} + \vartheta_j)) \delta(y) e^{il(k_{\beta,r,z} + \vartheta_j)} e^{\pm i(\nu\theta_j - hk_{\beta,r,z} + \nu\xi_j \sin(2(k_{\beta,r,z} + \vartheta_j)))}} \\
&= e^{\pm i\nu\theta_j} e^{\pm ih\vartheta_j} \delta(y) \int \frac{dk_x}{2\pi} e^{ik_x x} \overline{e^{-ik_x a_{\beta,j} \cos(k_{\beta,r,z} + \vartheta_j)} e^{\pm i\nu\xi_j \sin(2(k_{\beta,r,z} + \vartheta_j))} e^{i(l\mp h)(k_{\beta,r,z} + \vartheta_j)}} \\
&= e^{\pm i\nu\theta_j} e^{\pm ih\vartheta_j} \delta(y) \int \frac{dk_x}{2\pi} e^{ik_x x} \sum_{n,m \in \mathbb{Z}} (-i)^n J_n(k_x a_{\beta,j}) J_m(\nu\xi_j) \overline{e^{i(l\mp h \pm n \pm 2m)(k_{\beta,r,z} + \vartheta_j)}} \\
&= e^{\pm i\nu\theta_j} e^{\pm ih\vartheta_j} \delta(y) \int \frac{dk_x}{2\pi} e^{ik_x x} \sum_{\substack{n \in \mathbb{Z} \\ h-n\mp l \text{ even}}} (-i)^n J_n(k_x a_{\beta,j}) J_{\frac{h-n\mp l}{2}}(\nu\xi_j) \\
&= e^{\pm i\nu\theta_j} e^{\pm ih\vartheta_j} \delta(y) \sum_{\substack{n \in \mathbb{Z} \\ h-n\mp l \text{ even}}} J_{\frac{h-n\mp l}{2}}(\nu\xi_j) \left[\frac{1}{a_{\beta,j}} \int \frac{d\kappa}{2\pi i^n} J_n(\kappa) e^{i\kappa \left(\frac{x}{a_{\beta,j}}\right)} \right] \\
&= e^{\pm i\nu\theta_j} e^{\pm ih\vartheta_j} \sum_{\substack{n \in \mathbb{Z} \\ h-n\mp l \text{ even}}} J_{\frac{h-n\mp l}{2}}(\nu\xi_j) \frac{1}{a_{\beta,j}} \mathcal{C}_n \left(\frac{x}{a_{\beta,j}} \right) \delta(y) \\
&\simeq e^{\pm i\nu\theta_j} e^{\pm ih\vartheta_j} \sum_{\substack{n \in \mathbb{Z} \\ h-n\mp l \text{ even}}} J_{\frac{h-n\mp l}{2}}(h\xi_r) \frac{1}{a_{\beta,r}} \mathcal{C}_n \left(\frac{x}{a_{\beta,r}} \right) \delta(y).
\end{aligned} \tag{A5}$$

In Eq. (A5) we use a number of assumptions justified in the main text. We assume θ_j and ϑ_j are slowly varying over one betatron period which allows $e^{\pm i\nu\theta_j}$ and $e^{\pm ih\vartheta_j}$ to be taken out of the period average in the third line. We assume $\eta, \delta, \Delta\nu \ll 1$ and then ignore subleading order terms which allows us to replace the particle j values of ξ and a_β with the reference particle values in the last line. The main result of this section follows directly from Eq. (A5) and is

$$\begin{aligned}
& \overline{\delta^2(\mathbf{x}_\perp - \mathbf{x}_{\perp,j}) \sin(k_{\beta,r,z} + \vartheta_j) e^{\pm i\nu k_{1,r}\zeta_j} e^{\pm i\Delta\nu k_{\beta,r,z}}} \\
&\simeq \mp \frac{i}{2} e^{\pm i\nu\theta_j} e^{\pm ih\vartheta_j} [\text{JJ}]_h \mathcal{W}_h(\mathbf{x}_\perp)
\end{aligned} \tag{A6}$$

where we have defined

$$\mathcal{W}_h(\mathbf{x}_\perp) = \sum_{\substack{n \in \mathbb{Z} \\ h-n \text{ odd}}} \frac{[\text{JJ}]_{h-n}}{[\text{JJ}]_h} \frac{1}{a_{\beta,r}} \mathcal{C}_n \left(\frac{x}{a_{\beta,r}} \right) \delta(y) \tag{A7}$$

and

$$[\text{JJ}]_n = J_{\frac{n-1}{2}}(h\xi_r) - J_{\frac{n+1}{2}}(h\xi_r). \tag{A8}$$

where $n \in \mathbb{Z}$. Plots of the x part of $\mathcal{W}_h(\mathbf{x}_\perp)$ for $h = 1 \dots 4$ are shown in Figure 8. $\mathcal{W}_h(\mathbf{x}_\perp)$ obeys the normalization condition

$$\int d^2 \mathbf{x}_\perp \mathcal{W}_h(\mathbf{x}_\perp) = \begin{cases} 0 & h \text{ even} \\ 1 & h \text{ odd} \end{cases}. \tag{A9}$$

Appendix B: \mathcal{C}_n Functions

For integer n we define the function \mathcal{C}_n as

$$\mathcal{C}_n(x) \equiv \begin{cases} \frac{T_n(x)}{\pi\sqrt{1-x^2}} & |x| < 1 \\ 0 & |x| \geq 1. \end{cases} \tag{B1}$$

The first five \mathcal{C}_n are plotted in Figure 9. \mathcal{C}_n are orthogonal functions with respect to the weight $w(x) = \sqrt{1-x^2}$. These functions satisfy the identity $\mathcal{C}_{-n}(x) = \mathcal{C}_n(x)$. \mathcal{C}_n is an even function for even n and is an odd function for odd n . We note

$$\begin{aligned}
& \int_{-\infty}^{\infty} dx \mathcal{C}_n(x) = \int_{-1}^1 dx \mathcal{C}_n(x) \\
&= \frac{1}{\pi} \int_{-1}^1 dx \frac{T_n(x) T_0(x)}{\sqrt{1-x^2}} = \delta_{n,0}
\end{aligned} \tag{B2}$$

where the last integral was evaluated using the Chebyshev polynomial orthogonality identity [59, Table 18.3.1]. We now evaluate the integral

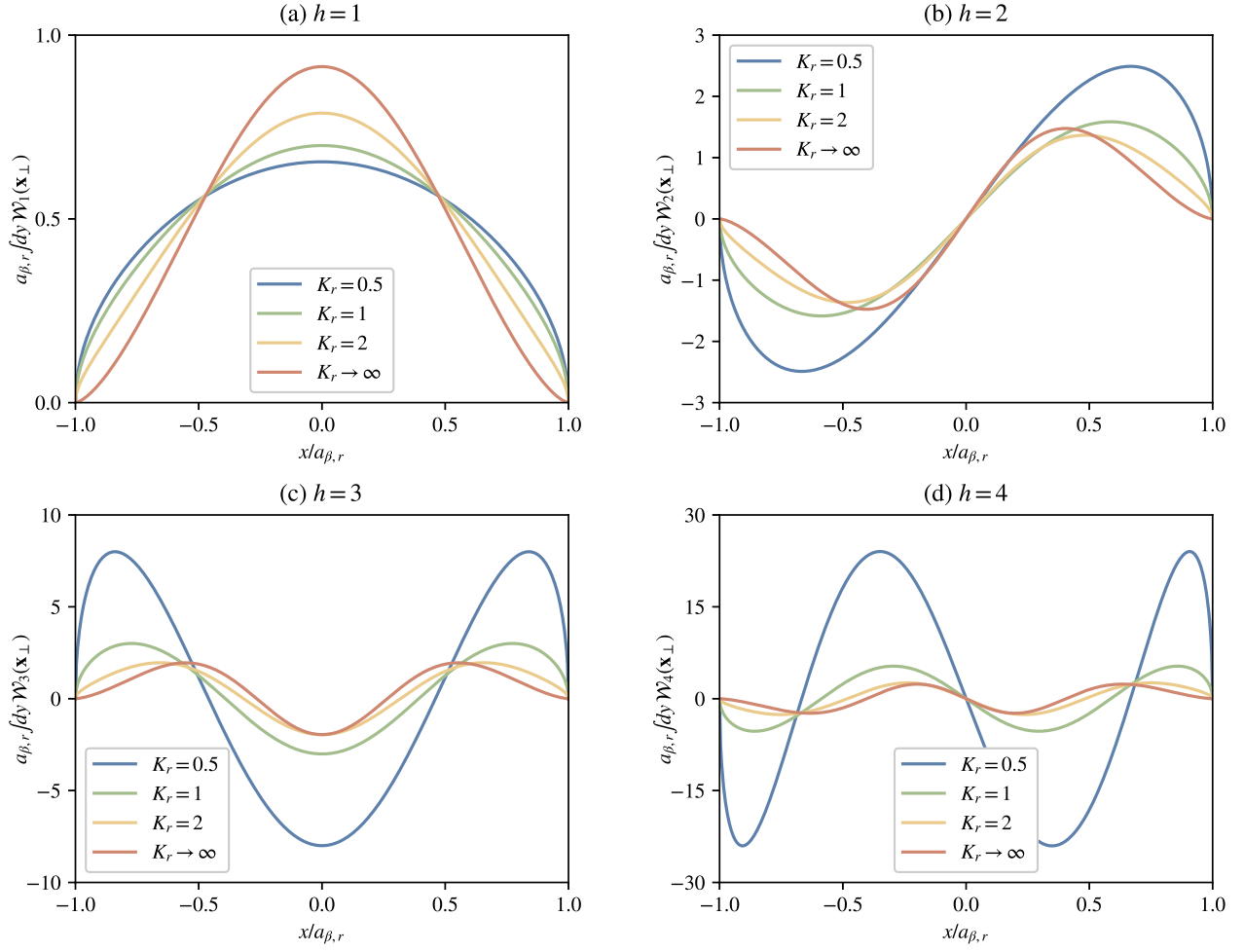


FIG. 8. Plots of $a_{\beta,r} \int dy \mathcal{W}_h(\mathbf{x}_\perp)$ for various values of K_r and h .

$$\begin{aligned}
& \int_{-\infty}^{\infty} \frac{d\kappa}{2\pi i^n} e^{i\kappa x} J_n(\kappa) \\
&= \int_{-\infty}^{\infty} \frac{d\kappa}{2\pi i^n} e^{i\kappa x} \left[\frac{i^{-n}}{\pi} \int_0^\pi d\theta e^{i\kappa \cos(\theta)} \cos(n\theta) \right] \\
&= \frac{(-1)^n}{\pi} \int_0^\pi d\theta \cos(n\theta) \int_{-\infty}^{\infty} \frac{d\kappa}{2\pi} e^{i\kappa(x+\cos(\theta))} \\
&= \frac{(-1)^n}{\pi} \int_0^\pi d\theta \cos(n\theta) \delta(x + \cos(\theta)) \\
&= \frac{(-1)^n}{\pi} \int_{-1}^1 dy \frac{\cos(n \cos^{-1}(y)) \delta(x+y)}{\sqrt{1-y^2}} \\
&= \begin{cases} \frac{(-1)^n \cos(n \cos^{-1}(x+\pi))}{\pi \sqrt{1-x^2}} & |x| < 1 \\ 0 & |x| \geq 1 \end{cases} \\
&= \begin{cases} \frac{\cos(n \cos^{-1}(x))}{\pi \sqrt{1-x^2}} & |x| < 1 \\ 0 & |x| \geq 1 \end{cases} \\
&= \begin{cases} \frac{T_n(x)}{\pi \sqrt{1-x^2}} & |x| < 1 \\ 0 & |x| \geq 1 \end{cases} \\
&= \mathcal{C}_n(x)
\end{aligned} \tag{B3}$$

where we have made use of [59, (10.9.2),(18.5.1)].

Appendix C: Slowly Varying Envelope Approximation

The field $a(\mathbf{x}_\perp, \zeta, z)$ can be written as a Fourier transform

$$a(\mathbf{x}_\perp, \zeta, z) = \int d\nu e^{i\nu k_{1,r} \zeta} \tilde{a}(\mathbf{x}_\perp, \nu, z) \tag{C1}$$

where $\nu \equiv k/k_1$ is the spatial frequency normalized to the fundamental. Because $a(\mathbf{x}_\perp, \zeta, z)$ is a physical field and cannot have an imaginary component, the spectrum must satisfy $\tilde{a}^*(\mathbf{x}_\perp, -\nu, z) = \tilde{a}(\mathbf{x}_\perp, \nu, z)$. This means that

$$a(\mathbf{x}_\perp, \zeta, z) = \int_0^\infty d\nu e^{i\nu k_{1,r} \zeta} \tilde{a}(\mathbf{x}_\perp, \nu, z) + \text{c.c.} \tag{C2}$$

One of the main assumptions used in this paper is that the radiation field spectrum consists of distinct peaks at

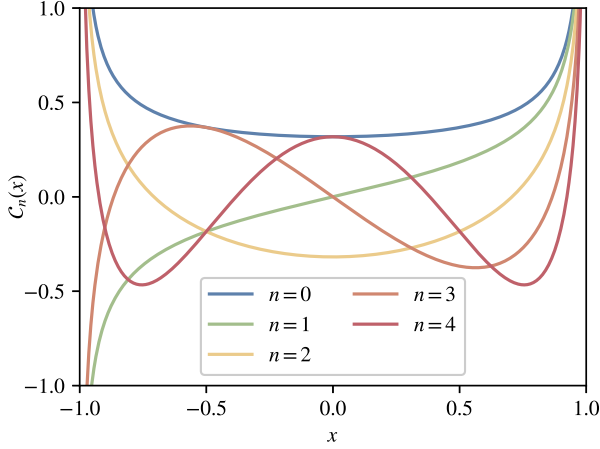


FIG. 9. Plot of the first five C_n functions discussed in Appendix B.

frequencies that are integer harmonics of the fundamental. With this assumption we define

$$\mathcal{A}_h(\mathbf{x}_\perp, \nu, z) \equiv \begin{cases} e^{-i\Delta\nu k_{\beta,r} z} \tilde{a}(\mathbf{x}_\perp, \nu, z) & \nu \approx h \\ 0 & \nu \not\approx h \end{cases} \quad (\text{C3})$$

where $\Delta\nu \equiv \nu - h \ll 1$. $\mathcal{A}_h(\mathbf{x}_\perp, \nu, z)$ contains only the h -th peak of the spectrum of the field. Using Eqs. (C2) and (C3) and defining the pondermotive phase coordinate $\theta(\zeta, z) \equiv k_{\beta,r} z + k_{1,r} \zeta$ we rewrite the field as

$$\begin{aligned} a(\mathbf{x}_\perp, \zeta, z) &= \\ &= \int_0^\infty d\nu e^{i\nu k_{1,r} \zeta} \tilde{a}(\mathbf{x}_\perp, \nu, z) + \text{c.c.} \\ &= \int_0^\infty d\nu e^{i\nu k_{1,r} \zeta} \left[\sum_{h \in \mathbb{Z}} e^{i\Delta\nu k_{\beta,r} z} \mathcal{A}_h(\mathbf{x}_\perp, \nu, z) \right] + \text{c.c.} \\ &= \sum_{h \in \mathbb{N}^+} \left[\int_{\nu \approx h} d\nu e^{i\Delta\nu \theta} \mathcal{A}_h(\mathbf{x}_\perp, \nu, z) \right] e^{ihk_1 \zeta} + \text{c.c.} \\ &= \sum_{h \in \mathbb{N}^+} a_{\text{sv},h}(\mathbf{x}_\perp, \theta, z) e^{ihk_1 \zeta} + \text{c.c.} \end{aligned} \quad (\text{C4})$$

which is a sum of slowly varying (independent of ζ) envelope functions

$$a_{\text{sv},h}(\mathbf{x}_\perp, \theta, z) \equiv \int_{\nu \approx h} d\nu e^{i\Delta\nu \theta} \mathcal{A}_h(\mathbf{x}_\perp, \nu, z) \quad (\text{C5})$$

multiplying carrier waves at integer harmonics of the fundamental. The field consists of distinct spectral peaks at integer harmonics of the fundamental frequency is equivalent to the slowly varying envelope approximation—that the field is the sum of slowly varying envelope functions multiplying carrier waves at integer harmonics of the fundamental.

Appendix D: Energy Conservation of the Maxwell-Klimontovich Equations

We show that the Maxwell-Klimontovich equations in Eq. (19) conserve energy. The energy in the electromagnetic field per unit transverse area is given by

$$\begin{aligned} \mathcal{U}_{\perp, \text{EM}}(\mathbf{x}_\perp, z) &= \frac{I_A}{8\pi} \int d\zeta (|\mathbf{E}|^2 + |\mathbf{B}|^2) \\ &\simeq \frac{I_A}{4\pi} \int d\zeta \left| \frac{\partial}{\partial \zeta} a(\mathbf{x}_\perp, \zeta, z) \right|^2 \\ &= \frac{I_A}{4\pi} \int d\zeta \left(\int d\nu i\nu k_{1,r} \tilde{a}(\mathbf{x}_\perp, \nu, z) e^{i\nu k_{1,r} \zeta} \right) \\ &\quad \times \left(\int d\nu' (-i)\nu' k_{1,r} \tilde{a}^*(\mathbf{x}_\perp, \nu', z) e^{-i\nu' k_{1,r} \zeta} \right) \\ &= \frac{k_{1,r} I_A}{2} \int d\nu \nu^2 |\tilde{a}(\mathbf{x}_\perp, \nu, z)|^2 \\ &= k_{1,r} I_A \int_0^\infty d\nu \nu^2 |\tilde{a}(\mathbf{x}_\perp, \nu, z)|^2. \end{aligned} \quad (\text{D1})$$

The total energy in the electromagnetic field is

$$\begin{aligned} \mathcal{E}_{\text{EM}}(z) &= \int d^2 \mathbf{x}_\perp \mathcal{U}(\mathbf{x}_\perp, z) \\ &= k_{1,r} I_A \int_0^\infty d\nu \nu^2 \int d^2 \mathbf{x}_\perp |\tilde{a}(\mathbf{x}_\perp, \nu, z)|^2. \end{aligned} \quad (\text{D2})$$

The change in this quantity with respect to z is

$$\begin{aligned}
\frac{d\mathcal{E}_{\text{EM}}}{dz} &= k_{1,r} I_A \int_0^\infty d\nu \nu^2 \int d^2\mathbf{x}_\perp \tilde{a}^*(\mathbf{x}_\perp, \nu, z) \frac{\partial}{\partial z} \tilde{a}(\mathbf{x}_\perp, \nu, z) + \text{c.c.} \\
&= k_{1,r} I_A \sum_{h \in \mathbb{N}^+} \int_{\nu \approx h} d\nu \nu^2 \int d^2\mathbf{x}_\perp \mathcal{A}_h^*(\mathbf{x}_\perp, \nu, z) \left[\frac{\partial}{\partial z} + i\Delta\nu k_{\beta,r} \right] \mathcal{A}_h(\mathbf{x}_\perp, \nu, z) + \text{c.c.} \\
&= k_{1,r} I_A \sum_{h \in \mathbb{N}^+} \int_{\nu \approx h} d\nu \nu^2 \int d^2\mathbf{x}_\perp \mathcal{A}_h^*(\mathbf{x}_\perp, \nu, z) \left[\frac{\partial}{\partial z} + i\Delta\nu k_{\beta,r} - \frac{i}{2\nu k_{1,r}} \nabla_\perp^2 \right] \mathcal{A}_h(\mathbf{x}_\perp, \nu, z) + \text{c.c.} \\
&= - \sum_{h \in \mathbb{N}^+} \int_{\nu \approx h} d\nu \frac{\nu k_{1,r} K_r [\text{JJ}]_h N_{\lambda_{1,r}}}{4\pi\gamma_r} \int d^2\mathbf{x}_\perp \mathcal{A}_h^*(\mathbf{x}_\perp, \nu, z) \mathcal{W}_h(\mathbf{x}_\perp) \iiint d\eta d\delta d\vartheta d\theta e^{-i\nu\theta} e^{-ih\vartheta} f(\eta, \delta, \vartheta, \theta, z) + \text{c.c.} \\
&= - \frac{N_{\lambda_{1,r}} \gamma_r}{2\pi} \iiint d\eta d\delta d\vartheta d\theta \left[\sum_{h \in \mathbb{N}^+} \int_{\nu \approx h} d\nu \frac{\nu k_{1,r} K_r [\text{JJ}]_h}{2\gamma_r^2} e^{ih\vartheta} e^{i\nu\theta} \int d^2\mathbf{x}_\perp \mathcal{W}_h(\mathbf{x}_\perp) \mathcal{A}_h(\mathbf{x}_\perp, \nu, z) + \text{c.c.} \right] f(\eta, \delta, \vartheta, \theta, z) \\
&= \frac{N_{\lambda_{1,r}} \gamma_r}{2\pi} \iiint d\eta d\delta d\vartheta d\theta \eta \left[\sum_{h \in \mathbb{N}^+} \int_{\nu \approx h} d\nu \frac{\nu k_{1,r} K_r [\text{JJ}]_h}{2\gamma_r^2} e^{ih\vartheta} e^{i\nu\theta} \int d^2\mathbf{x}_\perp \mathcal{W}_h(\mathbf{x}_\perp) \mathcal{A}_h(\mathbf{x}_\perp, \nu, z) + \text{c.c.} \right] \frac{\partial}{\partial \eta} f(\eta, \delta, \vartheta, \theta, z) \\
&= \frac{N_{\lambda_{1,r}} \gamma_r}{2\pi} \iiint d\eta d\delta d\vartheta d\theta \eta \eta' \frac{\partial}{\partial \eta} f(\eta, \delta, \vartheta, \theta, z) \\
&= \frac{N_{\lambda_{1,r}} \gamma_r}{2\pi} \iiint d\eta d\delta d\vartheta d\theta \eta \left[\eta' \left(\frac{\partial}{\partial \eta} + \frac{1 + K_r^2}{2K_r^2} \frac{\partial}{\partial \delta} \right) + 2k_{\beta,r} \left(\eta - \frac{K_r^2}{2 + K_r^2} \delta \right) \frac{\partial}{\partial \theta} - \frac{1}{2} k_{\beta,r} \eta \frac{\partial}{\partial \vartheta} \right] f(\eta, \delta, \vartheta, \theta, z) \\
&= - \frac{N_{\lambda_{1,r}} \gamma_r}{2\pi} \iiint d\eta d\delta d\vartheta d\theta \eta \frac{\partial}{\partial z} f(\eta, \delta, \vartheta, \theta, z) \\
&= - \frac{d}{dz} \sum_{j=1}^{N_e} \gamma_j
\end{aligned} \tag{D3}$$

which is exactly negative the change in the kinetic energy of the electrons in the bunch. Thus the sum of the potential energy in the field and the kinetic energy in the particles in the bunch is constant as expected, and so energy is conserved.

Appendix E: Computing $\mathcal{X}_h(\hat{z}, \hat{z}')$ and $\mathcal{V}(\mu)$

In this Appendix we compute, for an electron bunch background distribution \hat{f}_0 with Gaussian energy detuning $\hat{\eta}$ and undulator parameter $\hat{\delta}$ distributions, the functions $\mathcal{X}_h(\hat{z}, \hat{z}')$ defined in Eq. (31) and appearing in the ICL initial value problem Eq. (30) and $\mathcal{V}(\mu)$ defined in Eq. (43) and appearing in the dispersion relation Eq. (42). After this we take the limit as the spread in $\hat{\eta}$ and $\hat{\delta}$ go to zero to obtain $\mathcal{X}(\hat{z}, \hat{z}')$ and $\mathcal{V}(\mu)$ for a ‘‘cold’’ bunch. We assume that the background beam distribution \hat{f}_0 has no dependence on \hat{z} and that there are no correlations between the betatron phase detuning ϑ and $\hat{\eta}$ or $\hat{\delta}$. With these assumptions the background beam distribution can be written

$$\hat{f}_0(\hat{\eta}, \hat{\delta}, \vartheta, \hat{z}) = \hat{f}_{0,\hat{\eta}\hat{\delta}}(\hat{\eta}, \hat{\delta}) \hat{f}_{0,\vartheta}(\vartheta) \tag{E1}$$

where we choose the normalization such that $\iint d\hat{\eta} d\hat{\delta} \hat{f}_{0,\hat{\eta}\hat{\delta}}(\hat{\eta}, \hat{\delta}) = 1$ and $\int d\vartheta \hat{f}_{0,\vartheta}(\vartheta) = 1$. Because

the ϑ integration in Eqs. (31) and (43) can be carried out using this normalization condition and Eq. (E1), the physics is independent of the ϑ distribution. For a Gaussian distribution in $\hat{\eta}$ and $\hat{\delta}$,

$$\hat{f}_{0,\hat{\eta}\hat{\delta}}(\hat{\eta}, \hat{\delta}) = \frac{e^{-\frac{(\hat{\eta}-\hat{\eta}_0)^2}{2\sigma_\eta^2}}}{\sqrt{2\pi}\sigma_\eta} \times \frac{e^{-\frac{(\hat{\delta}-\hat{\delta}_0)^2}{2\sigma_\delta^2}}}{\sqrt{2\pi}\sigma_\delta}. \tag{E2}$$

First we compute $\mathcal{X}_h(\hat{z}, \hat{z}')$ using Eq. (31). Plugging in Eqs. (E1) and (E2) and making the substitutions $\hat{\eta} \equiv \hat{\eta}_0 + u\sigma_\eta$ and $\hat{\delta} \equiv \hat{\delta}_0 + v\sigma_\delta$ we obtain

$$\begin{aligned}
\mathcal{X}_h(\hat{z}, \hat{z}') &= - \frac{e^{i(\hat{z}-\hat{z}') \left[-\left(\frac{3}{4}h+\Delta\nu\right)\hat{\eta}_0 + (h+\Delta\nu)\frac{K_r^2}{2+K_r^2}\hat{\delta}_0 \right]}}{2\mathcal{I}} \frac{[\text{JJ}]_h^2}{[\text{JJ}]_1^2} \times \\
&\times \iint dudv \left(\frac{u}{\sigma_\eta} + \frac{1+K_r^2}{2K_r^2} \frac{v}{\sigma_\delta} \right) e^{-\frac{1}{2}(u^2+v^2)} \times \\
&\times e^{i(\hat{z}-\hat{z}') \left[-\left(\frac{3}{4}h+\Delta\nu\right)\sigma_\eta u + (h+\Delta\nu)\frac{K_r^2}{2+K_r^2}\sigma_\delta v \right]}
\end{aligned} \tag{E3}$$

which can be integrated to give

$$\mathcal{X}_h(\hat{z}, \hat{z}') = i\pi A(\hat{z} - \hat{z}') e^{-i(\hat{z}-\hat{z}')\mu_0} e^{-\frac{1}{2}(\hat{z}-\hat{z}')^2\Sigma^2} \tag{E4}$$

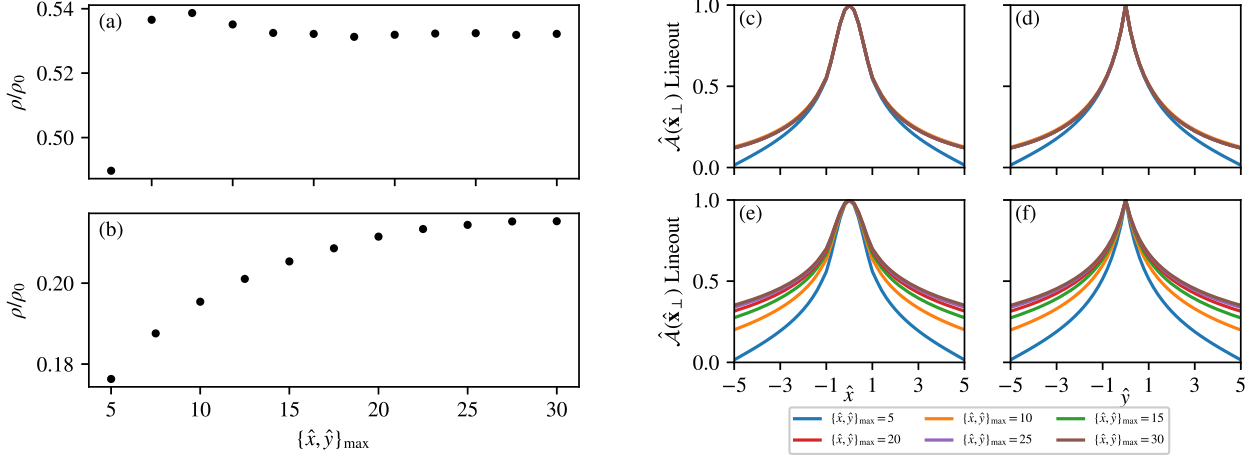


FIG. 10. Simulation box size convergence scan. Left plots show relative gain parameter ρ/ρ_0 as a function of $\{\hat{x}, \hat{y}\}_{\max}$ for $\rho_0 = 0.01$ (a) and $\rho_0 = 0.001$ (b). $\{\hat{x}, \hat{y}\}_{\max} = \hat{x}_{\max} = \hat{y}_{\max} = -\hat{x}_{\min} = -\hat{y}_{\min}$ is half the side length of the square transverse area over which the algorithm solves Eq. (45). Right plots show x (c,e) and y (d,f) lineouts of the transverse radiation profiles for $\rho = 0.01$ (c,d) and $\rho = 0.001$ (e,f). Colors within these plots indicate different values of $\{\hat{x}, \hat{y}\}_{\max}$.

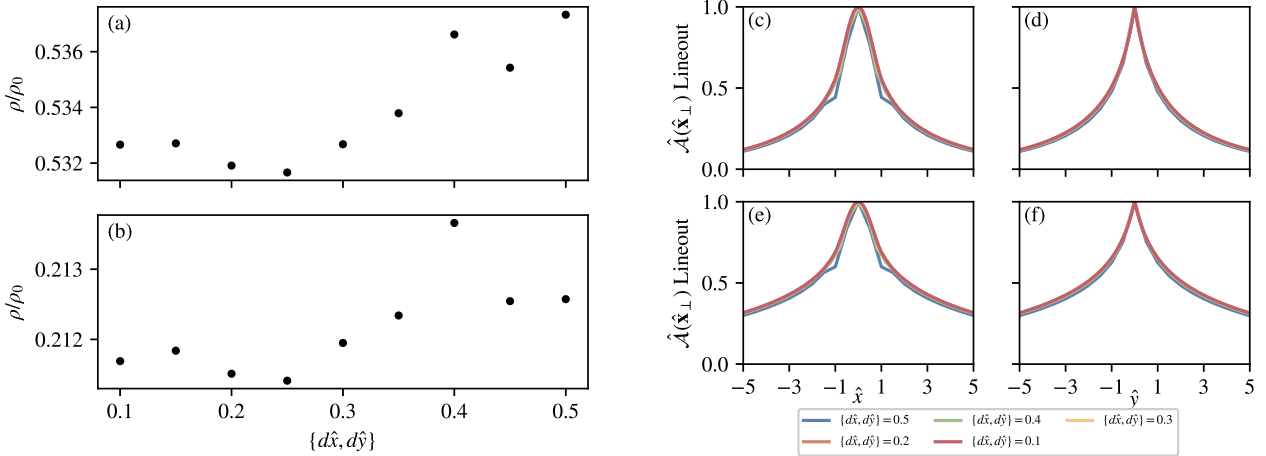


FIG. 11. Transverse grid size convergence scan. Left plots show relative gain parameter ρ/ρ_0 as a function of transverse cell size $\{d\hat{x}, d\hat{y}\}$ for $\rho_0 = 0.01$ (a) and $\rho_0 = 0.001$ (b). Right plots show x (c,e) and y (d,f) lineouts of the transverse radiation profiles for $\rho = 0.01$ (c,d) and $\rho = 0.001$ (e,f). Colors within these plots indicate different values of $\{d\hat{x}, d\hat{y}\}$.

where

$$\begin{aligned}
 A &\equiv \left(h + \frac{2(3 + K_r^2)}{4 + K_r^2} \Delta\nu \right) \frac{[\text{JJ}]_h^2}{[\text{JJ}]_1^2} \\
 \mu_0 &\equiv \left(\frac{3}{4}h + \Delta\nu \right) \hat{\eta}_0 - (h + \Delta\nu) \frac{K_r^2}{2 + K_r^2} \hat{\delta}_0 \\
 \Sigma &\equiv \sqrt{\Sigma_{\hat{\eta}}^2 + \Sigma_{\hat{\delta}}^2} \\
 \Sigma_{\hat{\eta}} &\equiv \left(\frac{3}{4}h + \Delta\nu \right) \sigma_{\hat{\eta}} \\
 \Sigma_{\hat{\delta}} &\equiv (h + \Delta\nu) \frac{K_r^2}{2 + K_r^2} \sigma_{\hat{\delta}}.
 \end{aligned} \tag{E5}$$

Next we compute $\mathcal{V}(\mu)$ in an analogous way by plugging Eqs. (E1) and (E2) into Eq. (43) and making the same to get

$$\mathcal{V}(\mu) = \frac{A}{2\pi} \iint dudv \frac{e^{-\frac{u^2+v^2}{2}}}{(\Delta\mu - u\Sigma_{\hat{\eta}} + v\Sigma_{\hat{\delta}})^2} \tag{E6}$$

where $\Delta\mu \equiv \mu - \mu_0$. This can be further simplified by making the transformation $u = \frac{\Sigma}{2\Sigma_{\hat{\eta}}}(w+x)$, $v = \frac{\Sigma}{2\Sigma_{\hat{\delta}}}(w-x)$ and performing the w integral to give

$$\mathcal{V}(\mu) = \frac{A}{(\Delta\mu)^2} I \left(\frac{\Sigma}{\Delta\mu} \right) \tag{E7}$$

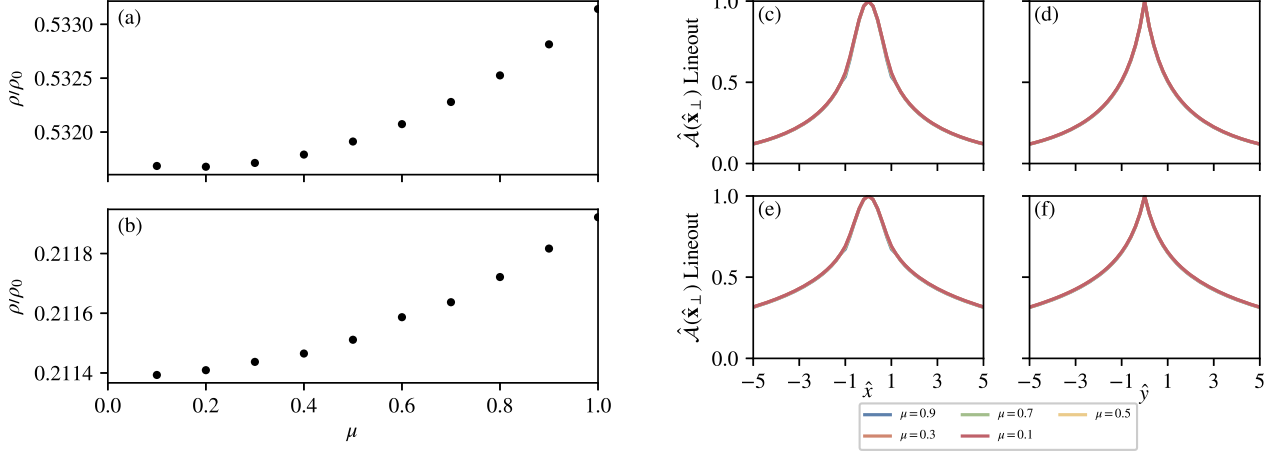


FIG. 12. Normalized \hat{z} step size convergence scan. Left plots show relative gain parameter ρ/ρ_0 as a function of $\mu = d\hat{z}/(2\mathcal{F}_D d\hat{x}^2) = d\hat{z}/(2\mathcal{F}_D d\hat{y}^2)$ for $\rho_0 = 0.01$ (a) and $\rho_0 = 0.001$ (b). Right plots show x (c,e) and y (d,f) lineouts of the transverse radiation profiles for $\rho_0 = 0.01$ (c,d) and $\rho_0 = 0.001$ (e,f). Colors within these plots indicate different values of μ .

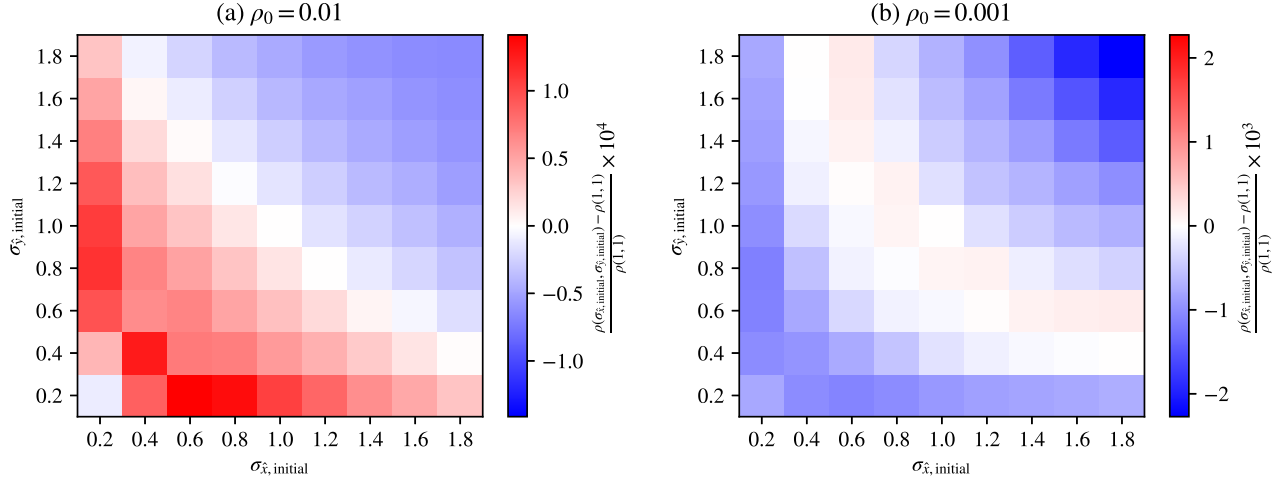


FIG. 13. Sensitivity of ρ to the x and y sizes of the Gaussian seed radiation field. Plots show the relative error of $\rho(\sigma_{\hat{x},\text{initial}}, \sigma_{\hat{y},\text{initial}})$ relative to $\rho(\sigma_{\hat{x},\text{initial}} = 1, \sigma_{\hat{y},\text{initial}} = 1)$ used in the “base” simulation for $\rho_0 = 0.01$ (a) and $\rho_0 = 0.001$ (b). Note the 10^4 (a) and 10^3 (b) scaling factor in the colorbar.

where

$$I(y) = \frac{1}{\sqrt{2\pi}} \int dx \frac{e^{-\frac{1}{2}x^2}}{(1-xy)^2}. \quad (\text{E8})$$

While it is possible to write the above in terms of complex error functions, we find the given form to be more useful.

Now that we have derived Eqs. (E4) and (E7) which give the $\mathcal{X}(\hat{z}, \hat{z}')$ and $\mathcal{V}(\mu)$ functions respectively for a bunch with Gaussian distributions in $\hat{\eta}$ and $\hat{\delta}$, we take the limit $\sigma_{\hat{\eta}}, \sigma_{\hat{\delta}} \rightarrow 0$ to compute the functions for a “cold” bunch $\hat{f}_{0,\hat{\eta}\hat{\delta}}(\hat{\eta}, \hat{\delta}) = \delta(\hat{\eta} - \hat{\eta}_0)\delta(\hat{\delta} - \hat{\delta}_0)$:

$$\mathcal{X}(\hat{z}, \hat{z}') = i\pi A(\hat{z} - \hat{z}')e^{-i(\hat{z} - \hat{z}')\mu_0} \quad (\text{E9})$$

$$\mathcal{V}(\mu) = A/(\Delta\mu)^2 \quad (\text{E10})$$

Appendix F: Crank-Nicholson Code Convergence

The Crank-Nicholson code discussed in Section III depends on a number of nonphysical parameters: the location of the transverse boundary $\hat{x}_{\text{max}} (= \hat{y}_{\text{max}} = -\hat{x}_{\text{min}} = -\hat{y}_{\text{min}})$, the transverse cell size $d\hat{x} (= d\hat{y})$, the parameter $\mu (= \mu_x = \mu_y)$ which the code uses to calculate the \hat{z} step size, and the standard deviations $\sigma_{\hat{x},\text{initial}}$ and $\sigma_{\hat{y},\text{initial}}$ of the initial Gaussian radiation field. Here we demonstrate the convergence (or, in the case of $\sigma_{\hat{x},\text{initial}}$ and $\sigma_{\hat{y},\text{initial}}$, insensitivity) of the simulation results with respect to

these non-physical parameters. We use the physical parameters $h = 1$, $K_r \rightarrow \infty$, $\hat{\Delta}\nu = 0$, $\Sigma = 0$, and $\rho_0 = 0.01$ from the ‘‘base’’ simulation from Section IV. Because we find that some quantities converge slower for smaller ρ , we also include convergence scans for a second simulation with these same parameters except $\rho_0 = 0.001$. For the non-physical parameters, we start with $\hat{x}_{\text{max}} = 20$, $d\hat{x} = 0.2$, $\mu = 0.5$, and $\sigma_{\hat{x},\text{initial}} = \sigma_{\hat{y},\text{initial}} = 1$ and vary each individually.

For the first convergence scan we vary the value of \hat{x}_{max} . The results are shown in Figure 10, which demonstrate clear convergence as the simulation box size increases. For $\rho_0 = 0.01$ ($\rho_0 = 0.001$), The value $\hat{x}_{\text{max}} = 20$ used in Section IV and in other convergence scans gives a value of ρ with a relative error of 0.053% (1.8%) compared to the $\hat{x}_{\text{max}} = 30$ simulation. We note faster convergence of the lineout for $\rho_0 = 0.01$ than for $\rho_0 = 0.001$. We suspect this is due to the wider beam in the latter case, although even in that case the lineout for $\hat{x}_{\text{max}} = 20$ is only marginally different than $\hat{x}_{\text{max}} = 30$.

The next scan is over $d\hat{x}$ and is shown in Figure 11. These results show relatively straightforward convergence with the value of ρ having only a 0.14% (0.085%) error at the value $d\hat{x} = 0.2$ used in Section IV and other convergence scans compared to the more accurate $d\hat{x} = 0.1$.

The next convergence scan is over μ and the results are shown in Figure 12. Again this shows straightforward convergence with the value $\mu = 0.5$ used in Section IV and other convergence scans yielding a value of ρ with a relative error of only 0.043% (0.056%) when compared to the more accurate simulation with $\mu = 0.1$. There is almost no noticeable difference in the lineout shapes for simulations with different values of μ .

While not technically a convergence scan, we ran a number of simulations with different values of $\sigma_{\hat{x},\text{initial}}$ and $\sigma_{\hat{y},\text{initial}}$ with the resulting values of ρ shown in Fig. (13). These results show that, as expected, the ICL gain parameter is only barely sensitive to the size of the seed radiation field with differences of at most a few tenths of a percent between simulations.

To summarize, we have demonstrated the convergence of two representative ICL simulations with respect to the nonphysical parameters \hat{x}_{max} , $d\hat{x}$, and μ , and the insensitivity of these simulations with respect to nonphysical parameters $\sigma_{\hat{x},\text{initial}}$ and $\sigma_{\hat{y},\text{initial}}$. This is a good indication that this algorithm behaves as we expect and the nonphysical parameters used in Section IV are adequate to accurately resolve the relevant physics.

Appendix G: Bunch Distribution Optimization

The normalized phase space distribution functions for the matched offset Gaussian, optimally mismatched offset Gaussian, and phase space annular sector bunches are

$$\begin{aligned} f_{\text{MOG}}(\tilde{\mathbf{x}}_{\perp}, \tilde{\mathbf{p}}_{\perp}) &= \frac{e^{-\frac{(\tilde{x}-\tilde{\mu})^2 + \tilde{y}^2 + \tilde{p}_x^2 + \tilde{p}_y^2}{2\tilde{\sigma}^2}}}{4\pi^2\tilde{\sigma}^4} \\ f_{\text{OMOG}}(\tilde{\mathbf{x}}_{\perp}, \tilde{\mathbf{p}}_{\perp}) &= \frac{e^{-\frac{(\tilde{x}-\tilde{\mu})^2}{2\tilde{\sigma}_x^2} - \frac{\tilde{y}^2}{2\tilde{\sigma}_y^2} - \frac{\tilde{p}_x^2}{2\tilde{\sigma}_{p_x}^2} - \frac{\tilde{p}_y^2}{2\tilde{\sigma}_{p_y}^2}}}{4\pi^2\tilde{\sigma}_x\tilde{\sigma}_y\tilde{\sigma}_{p_x}\tilde{\sigma}_{p_y}} \\ f_{\text{PSAS}}(\tilde{\mathbf{x}}_{\perp}, \tilde{\mathbf{p}}_{\perp}) &= \frac{1}{\Theta\tilde{\mu}\tilde{w}} \text{rect}\left(\frac{\sqrt{\tilde{x}^2 + \tilde{p}_x^2} - \tilde{\mu}}{\tilde{w}}\right) \times \\ &\times \text{rect}\left(\frac{\text{atan2}(\tilde{p}_x, \tilde{x})}{\Theta}\right) \frac{e^{-\frac{\tilde{y}^2}{2\tilde{\sigma}_y^2} - \frac{\tilde{p}_y^2}{2\tilde{\sigma}_{p_y}^2}}}{2\pi\tilde{\sigma}_y\tilde{\sigma}_{p_y}} \end{aligned} \quad (\text{G1})$$

where a tilde indicates a normalized quantity where positions are normalized to $a_{\beta,r}$ and momenta to K_r . Note that we are assuming these bunches are monochromatic. Computing moments of these distribution functions allows us to obtain the mean radiation wavelength for each case

$$\begin{aligned} \lambda_{1,b} &= \langle \lambda_1 \rangle = \left\langle \frac{\lambda_{\beta,r}}{2\gamma_r^2} \left(1 + K_r^2 \frac{\tilde{x}^2 + \tilde{y}^2 + \tilde{p}_x^2 + \tilde{p}_y^2}{2} \right) \right\rangle \\ &= \begin{cases} \frac{\lambda_{\beta,r}}{2\gamma_r^2} \left(1 + \frac{K_r^2(\tilde{\mu}^2 + 4\tilde{\sigma}^2)}{2} \right) & \text{MOG} \\ \frac{\lambda_{\beta,r}}{2\gamma_r^2} \left(1 + \frac{K_r^2(\tilde{\mu}^2 + \tilde{\sigma}_x^2 + \tilde{\sigma}_y^2 + \tilde{\sigma}_{p_x}^2 + \tilde{\sigma}_{p_y}^2)}{2} \right) & \text{OMOG} \\ \frac{\lambda_{\beta,r}}{2\gamma_r^2} \left(1 + \frac{K_r^2(\tilde{\mu}^2 + \frac{\tilde{w}^2}{4} + \tilde{\sigma}_y^2 + \tilde{\sigma}_{p_y}^2)}{2} \right) & \text{PSAS} \end{cases} \end{aligned} \quad (\text{G2})$$

as well as the wavelength spread

$$\begin{aligned} \sigma_{\lambda_{1,b}} &= \sqrt{\langle \lambda_1^2 \rangle - \langle \lambda_1 \rangle^2} \\ &= \begin{cases} \frac{\lambda_{\beta,r}K_r^2}{2\gamma_r^2} \sqrt{\tilde{\sigma}^2(\tilde{\mu}^2 + 2\tilde{\sigma}^2)} & \text{MOG} \\ \frac{\lambda_{\beta,r}K_r^2}{2\gamma_r^2} \sqrt{\tilde{\mu}^2\tilde{\sigma}_x^2 + \frac{\tilde{\sigma}_x^4 + \tilde{\sigma}_y^4 + \tilde{\sigma}_{p_x}^4 + \tilde{\sigma}_{p_y}^4}{2}} & \text{OMOG} \\ \frac{\lambda_{\beta,r}K_r^2}{2\gamma_r^2} \sqrt{\frac{\tilde{\mu}^2\tilde{w}^2}{12} + \frac{\tilde{\sigma}_y^4 + \tilde{\sigma}_{p_y}^4}{2}} & \text{PSAS} \end{cases} \end{aligned} \quad (\text{G3})$$

Next we compute the emittance for each of the three cases. Note that 2D emittances with a tilde are normalized to $a_{\beta,r}K_r$ and 4D emittances with a tilde are normalized to $a_{\beta,r}^2K_r^2$. For the x and y dimensions of the two Gaussian cases as well as the y dimension of the phase space annular sector case, there is no difference between the RMS emittance $\tilde{\epsilon}_{n,x,\text{RMS}} \equiv \sqrt{\det(\text{cov}(\tilde{x}, \tilde{p}_x))}$ and the geometric emittance $\tilde{\epsilon}_{n,x,\text{geometric}} \equiv \tilde{A}/\pi$ where \tilde{A} is the area of the distribution in normalized phase space (for Gaussian bunch distributions \tilde{A} is the area of an ellipse with semiaxes equal to $\tilde{\sigma}_x$ and $\tilde{\sigma}_{p_x}$). For the x dimension of the phase space annular sector case however, the RMS emittance

$$\begin{aligned} \tilde{\epsilon}_{n,x,\text{RMS}} &= \frac{\tilde{\mu}^2}{24\Theta} \left[\left(4 + \frac{\tilde{w}^2}{\tilde{\mu}^2} \right) (1 - \text{sinc}(\Theta)) \times \right. \\ &\times \left(9\Theta^2 \left(4 + \frac{\tilde{w}^2}{\tilde{\mu}^2} \right) (1 + \text{sinc}(\Theta)) + \right. \\ &\left. \left. + \left(12 + \frac{\tilde{w}^2}{\tilde{\mu}^2} \right)^2 (\cos(\Theta) - 1) \right) \right]^{\frac{1}{2}} \end{aligned} \quad (\text{G4})$$

is different than the geometric emittance $\tilde{\epsilon}_{n,x,\text{geometric}} = \Theta\tilde{\mu}\tilde{w}/\pi$. We use the geometric instead of the RMS emittance here because the geometric emittance goes to zero when $\tilde{w} \rightarrow 0$ while the rms emittance does not. The x and y emittances in each case are

$$\tilde{\epsilon}_{n,x}, \tilde{\epsilon}_{n,y} = \begin{cases} \tilde{\sigma}^2, & \tilde{\sigma}^2 & \text{MOG} \\ \tilde{\sigma}_x\tilde{\sigma}_{p_x}, & \tilde{\sigma}_y\tilde{\sigma}_{p_y} & \text{OMOG} \\ \Theta\tilde{\mu}\tilde{w}/\pi, & \tilde{\sigma}_y\tilde{\sigma}_{p_y} & \text{PSAS} \end{cases} \quad (\text{G5})$$

In each case, the distribution functions must obey the resonance condition $\lambda_{1,b} = \lambda_{1,r} = \frac{\lambda_{\beta,r}}{2\gamma_r^2} \left(1 + \frac{K_r^2}{2} \right)$. Using Eq. (G2) this allows us to solve for the offset $\tilde{\mu}$:

$$\tilde{\mu} = \begin{cases} \sqrt{1 - 4\tilde{\sigma}^2} & \text{MOG} \\ \sqrt{1 - \tilde{\sigma}_x^2 - \tilde{\sigma}_y^2 - \tilde{\sigma}_{p_x}^2 - \tilde{\sigma}_{p_y}^2} & \text{OMOG} \\ \sqrt{1 - \tilde{\sigma}_y^2 - \tilde{\sigma}_{p_y}^2 - \frac{\tilde{w}^2}{4}} & \text{PSAS} \end{cases} \quad (\text{G6})$$

Our goal is to for each of the three cases, for a given wavelength spread $\Delta\lambda_1$, find the parameters that minimize the emittance. Because there are two emittances (x and y), we choose the 4D emittance as the quantity to minimize

$$\begin{aligned} \tilde{\epsilon}_{n,4\text{D}} &= \tilde{\epsilon}_{n,x}\tilde{\epsilon}_{n,y} \\ &= \begin{cases} \tilde{\sigma}^4 & \text{MOG} \\ \tilde{\sigma}_x\tilde{\sigma}_y\tilde{\sigma}_{p_x}\tilde{\sigma}_{p_y} & \text{OMOG} \\ \frac{\Theta\tilde{w}\tilde{\sigma}_y\tilde{\sigma}_{p_y}}{\pi} \sqrt{1 - \tilde{\sigma}_y^2 - \tilde{\sigma}_{p_y}^2 - \frac{\tilde{w}^2}{4}} & \text{PSAS} \end{cases} \end{aligned} \quad (\text{G7})$$

This minimization is subject to the constraint that the wavelength spread of the bunch $\sigma_{\lambda_{1,b}}$ is equal to the given wavelength spread $\Delta\lambda_1$. To simplify the math we use the equivalent constraint $\sigma_{\lambda_{1,b}}^2 = (\Delta\lambda_1)^2$ during the calculation. With the help of Eqs. (G3) and (G6) this constraint is

$$\Delta^2 = \begin{cases} \tilde{\sigma}^2 (1 - 2\tilde{\sigma}^2) & \text{MOG} \\ \frac{1}{2} (\tilde{\sigma}_{p_x}^4 + \tilde{\sigma}_{p_y}^4 + \tilde{\sigma}_y^4 - \tilde{\sigma}_x^4) + & \text{OMOG} \\ + \tilde{\sigma}_x^2 (1 - \tilde{\sigma}_y^2 - \tilde{\sigma}_{p_x}^2 - \tilde{\sigma}_{p_y}^2) & \\ \frac{1}{2} (\tilde{\sigma}_y^4 + \tilde{\sigma}_{p_y}^4) + & \text{PSAS} \\ + \frac{\tilde{w}^2}{12} (1 - \tilde{\sigma}_y^2 - \tilde{\sigma}_{p_y}^2) - \frac{\tilde{w}^4}{48} & \end{cases} \quad (\text{G8})$$

where

$$\Delta \equiv \frac{1 + \frac{K_r^2}{2} \frac{\Delta\lambda_1}{\lambda_{1,r}}}{K_r^2 \frac{\Delta\lambda_1}{\lambda_{1,r}}} \quad (\text{G9})$$

We now consider each of the three cases individually. First, for the matched offset Gaussian distribution, no optimization needs to be performed as Eqs. (G8) fixes the only free parameter $\tilde{\sigma}$. For this case, the parameters and beam emittance are, in terms of wavelength spread,

$$\begin{aligned} \tilde{\mu} &= (1 - 8\Delta^2)^{\frac{1}{4}} \\ \tilde{\sigma} &= \frac{1}{2} \sqrt{1 - \sqrt{1 - 8\Delta^2}} \\ \tilde{\epsilon}_{n,x} = \tilde{\epsilon}_{n,y} &= \frac{1}{4} \left(1 - \sqrt{1 - 8\Delta^2} \right). \end{aligned} \quad (\text{G10})$$

To obtain the actual emittance constraint we write $\tilde{\epsilon}_{n,x}$ and $\tilde{\epsilon}_{n,y}$ in Eq. (G10) to leading order ($\Delta \sim \rho \ll 1$ unless K_r is small, but as discussed in Section II E the small K_r ICL is unfeasible due to diffraction) and then use the wavelength spread constraint $\Delta\lambda_1/\lambda_{1,r} \lesssim \rho$ to write, in non-normalized units,

$$\epsilon_{n,x}, \epsilon_{n,y} \lesssim \frac{\gamma\lambda_1}{\pi} \frac{1 + \frac{K^2}{2}}{K^2} \rho^2. \quad (\text{G11})$$

Next we consider the more complicated optimally mismatched case. We solved this optimization problem with Lagrange multipliers method in a computer algebra system. While there is an exact solution that can be written in terms of radicals, due to its excessive complexity we write the solution as a power series in Δ . For an optimally mismatched bunch, the bunch parameters and emittances in terms of Δ are

$$\begin{aligned} \tilde{\mu} &\simeq 1 - \frac{3}{\sqrt{10}}\Delta - \frac{77}{100}\Delta^2 - \frac{3}{4}\sqrt{\frac{5}{2}}\Delta^3 + O(\Delta^4) \\ \tilde{\sigma}_x &\simeq \sqrt{\frac{2}{5}}\Delta + \frac{12}{25}\Delta^2 + \frac{28}{25}\sqrt{\frac{2}{5}}\Delta^3 + O(\Delta^4) \\ \tilde{\sigma}_y = \tilde{\sigma}_{p_x} = \tilde{\sigma}_{p_y} &\simeq \left(\frac{2}{5}\right)^{\frac{1}{4}} \Delta^{\frac{1}{2}} + \frac{1}{5 \times 2^{\frac{1}{4}} \times 5^{\frac{3}{4}}} \Delta^{\frac{3}{2}} + \\ &+ \frac{39}{250 \times 2^{\frac{3}{4}} \times 5^{\frac{1}{4}}} \Delta^{\frac{5}{2}} + O\left(\Delta^{\frac{7}{2}}\right) \\ \tilde{\epsilon}_{n,x} &\simeq \left(\frac{2}{5}\right)^{\frac{3}{4}} \Delta^{\frac{3}{2}} + \frac{13}{25} \left(\frac{2}{5}\right)^{\frac{1}{4}} \Delta^{\frac{5}{2}} + \\ &+ \frac{623}{250 \times 2^{\frac{1}{4}} \times 5^{\frac{3}{4}}} \Delta^{\frac{7}{2}} + O\left(\Delta^{\frac{9}{2}}\right) \\ \tilde{\epsilon}_{n,y} &\simeq \sqrt{\frac{2}{5}}\Delta + \frac{2}{25}\Delta^2 + \frac{4}{25}\sqrt{\frac{2}{5}}\Delta^3 + O(\Delta^4) \end{aligned} \quad (\text{G12})$$

In the same way as before we compute the emittance constraint which is, in non-normalized units,

$$\begin{aligned}\epsilon_{n,x} &\lesssim \frac{\gamma\lambda_1}{\pi} \left(\frac{2}{5}\right)^{\frac{3}{4}} \left(\frac{1+\frac{K^2}{2}}{K^2}\right)^{\frac{1}{2}} \rho^{\frac{3}{2}} \\ \epsilon_{n,y} &\lesssim \frac{\gamma\lambda_1}{\pi} \sqrt{\frac{2}{5}}\rho.\end{aligned}\quad (\text{G13})$$

Finally we consider the phase space annular sector case. In this case we treat Θ as fixed rather than one of the parameters to optimize. Again we solved this optimization problem using Lagrange multipliers, although this time the exact solution is far simpler and so we don't compute a power series. The optimal parameters and emittances are

$$\begin{aligned}\tilde{w} &= \sqrt{2\left(1 - \sqrt{2}\Delta - \sqrt{1 - 2\sqrt{2}\Delta - 4\Delta^2}\right)} \\ \tilde{\mu} &= \sqrt{\frac{1 - \sqrt{2}\Delta + \sqrt{1 - 2\sqrt{2}\Delta - 4\Delta^2}}{2}} \\ \tilde{\sigma}_y &= \tilde{\sigma}_{p_y} = \frac{\sqrt{\Delta}}{2^{\frac{1}{4}}} \\ \tilde{\epsilon}_{n,x} &= \frac{\sqrt{6}\Theta\Delta}{\pi} \\ \tilde{\epsilon}_{n,y} &= \frac{\Delta}{\sqrt{2}}.\end{aligned}\quad (\text{G14})$$

The emittance constraint in non-normalized units is

$$\begin{aligned}\epsilon_{n,x} &\lesssim \frac{\gamma\lambda_1}{\pi} \frac{1}{\sqrt{2}}\rho \\ \epsilon_{n,y} &\lesssim \frac{\gamma\lambda_1}{\pi} \frac{\sqrt{6}\Theta}{\pi}\rho.\end{aligned}\quad (\text{G15})$$

-
- [1] K. Kim, Z. Huang, and R. Lindberg, *Synchrotron Radiation and Free-Electron Lasers* (Cambridge University Press, Cambridge, 2017).
- [2] C. Pellegrini, A. Marinelli, and S. Reiche, The physics of x-ray free-electron lasers, *Rev. Mod. Phys.* **88**, 015006 (2016).
- [3] Z. Huang and K.-J. Kim, Review of x-ray free-electron laser theory, *Phys. Rev. ST Accel. Beams* **10**, 034801 (2007).
- [4] C. Bostedt, S. Boutet, D. M. Fritz, Z. Huang, H. J. Lee, H. T. Lemke, A. Robert, W. F. Schlotter, J. J. Turner, and G. J. Williams, Linac Coherent Light Source: The first five years, *Rev. Mod. Phys.* **88**, 015007 (2016).
- [5] E. Esarey, C. B. Schroeder, and W. P. Leemans, Physics of laser-driven plasma-based electron accelerators, *Rev. Mod. Phys.* **81**, 1229 (2009).
- [6] K. Nakajima, Towards a table-top free-electron laser, *Nat. Phys.* **4**, 92 (2008).
- [7] S. Corde, K. Ta Phuoc, G. Lambert, R. Fitour, V. Malka, A. Rousse, A. Beck, and E. Lefebvre, Femtosecond x rays from laser-plasma accelerators, *Rev. Mod. Phys.* **85**, 1 (2013).
- [8] F. Albert *et al.*, Laser wakefield accelerator based light sources: potential applications and requirements, *Plasma Phys. Controlled Fusion* **56**, 084015 (2014).
- [9] F. Albert and A. G. R. Thomas, Applications of laser wakefield accelerator-based light sources, *Plasma Phys. Controlled Fusion* **58**, 103001 (2016).
- [10] F. Albert *et al.*, 2020 roadmap on plasma accelerators, *New J. Phys.* **23**, 031101 (2021).
- [11] W. Wang *et al.*, Free-electron lasing at 27 nanometres based on a laser wakefield accelerator, *Nature* **595**, 516 (2021).
- [12] M. Labat *et al.*, Seeded free-electron laser driven by a compact laser plasma accelerator, *Nat. Photonics* **17**, 150 (2023).
- [13] M. Tzoufras, W. Lu, F. S. Tsung, C. Huang, W. B. Mori, T. Katsouleas, J. Vieira, R. A. Fonseca, and L. O. Silva, Beam loading in the nonlinear regime of plasma-based acceleration, *Phys. Rev. Lett.* **101**, 145002 (2008).
- [14] A. R. Maier, A. Meseck, S. Reiche, C. B. Schroeder, T. Seggebrock, and F. Grüner, Demonstration scheme for a laser-plasma-driven free-electron laser, *Phys. Rev. X* **2**, 031019 (2012).
- [15] T. Seggebrock, A. R. Maier, I. Dornmair, and F. Grüner, Bunch decompression for laser-plasma driven free-electron laser demonstration schemes, *Phys. Rev. ST Accel. Beams* **16**, 070703 (2013).
- [16] Z. Huang, Y. Ding, and C. B. Schroeder, Compact x-ray free-electron laser from a laser-plasma accelerator using a transverse-gradient undulator, *Phys. Rev. Lett.* **109**, 204801 (2012).
- [17] X. Xu, J. Liu, T. Dalichaouch, F. S. Tsung, Z. Zhang, Z. Huang, M. J. Hogan, X. Yan, C. Joshi, and W. B. Mori, Attosecond x-ray free-electron lasers utilizing an optical undulator in a self-selection regime, *Phys. Rev. Accel. Beams* **27**, 011301 (2024).
- [18] C. Emma, X. Xu, A. Fisher, R. Robles, J. P. MacArthur, J. Cryan, M. J. Hogan, P. Musumeci, G. White, and A. Marinelli, Terawatt attosecond x-ray source driven by a plasma accelerator, *APL Photonics* **6**, 076107 (2021).
- [19] B. Malaca, M. Pardo, D. Ramsey, J. Pierce, K. Weichman, I. Andriyash, W. Mori, J. Palastro, R. Fonseca, and J. Vieira, Coherence and superradiance from a plasma-based quasiparticle accelerator, *Nat. Photonics* **18**, 39 (2023).
- [20] D. H. Whittum, A. M. Sessler, and J. M. Dawson, Ion-channel laser, *Phys. Rev. Lett.* **64**, 2511 (1990).
- [21] D. H. Whittum, *Theory of the ion channel laser*, Ph.D. thesis, University of California Berkeley (1990).
- [22] K.-R. Chen, T. Katsouleas, and J. Dawson, On the amplification mechanism of the ion-channel laser, *IEEE Trans.*

- Plasma Sci. **18**, 837 (1990).
- [23] K.-R. Chen, J. M. Dawson, A. T. Lin, and T. Katsouleas, Unified theory and comparative study of cyclotron masers, ion-channel lasers, and free electron lasers, *Phys. Fluids B* **3**, 1270 (1991).
- [24] D. Whittum, Electromagnetic instability of the ion-focused regime, *Phys. Fluids B* **4**, 730 (1992).
- [25] D. Whittum, K. Ebihara, S. Hiramatsu, J. Kishiro, T. Monaka, T. Ozaki, and K. Takayama, Experimental studies of microwave amplification in the ion-focused regime, *IEEE Trans. Plasma Sci.* **21**, 136 (1993).
- [26] H. Kupersmidt and A. Ron, One-particle theory of ion-channel laser, *IEEE Trans. Plasma Sci.* **22**, 674 (1994).
- [27] E. Esarey, B. A. Shadwick, P. Catravas, and W. P. Leemans, Synchrotron radiation from electron beams in plasma-focusing channels, *Phys. Rev. E* **65**, 056505 (2002).
- [28] I. Kostyukov, S. Kiselev, and A. Pukhov, X-ray generation in an ion channel, *Phys. Plasmas* **10**, 4818 (2003).
- [29] R. Bosch, Radially polarized ion channel laser, in *Proceedings of the 2005 Particle Accelerator Conference* (IEEE, New York, 2005) pp. 1526–1528.
- [30] C. S. Liu, V. K. Tripathi, and N. Kumar, Vlasov formalism of the laser driven ion channel x-ray laser, *Plasma Phys. Controlled Fusion* **49**, 325 (2007).
- [31] B. Ersfeld, R. Bonifacio, S. Chen, M. R. Islam, P. W. Smorenburg, and D. A. Jaroszynski, The ion channel free-electron laser with varying betatron amplitude, *New J. Phys.* **16**, 093025 (2014).
- [32] S. Chen, *FEL theory in the ion channel wiggler*, Ph.D. thesis, University of Strathclyde (2016), available online at <https://stax.strath.ac.uk/concern/theses/bk128995p>.
- [33] V. Shpakov, E. Chiadroni, A. Curcio, H. Fares, M. Ferrario, A. Marocchino, V. Petrillo, A. Rossi, and S. Romeo, Study of the beam tolerance for plasma based ion channel lasers, *Nucl. Instrum. Methods Phys. Res., Sect. B* **402**, 384 (2017).
- [34] X. Davoine, F. Fiúza, R. A. Fonseca, W. B. Mori, and L. O. Silva, Ion-channel laser growth rate and beam quality requirements, *J. Plasma Phys.* **84**, 905840304 (2018).
- [35] M. Litos, R. Ariniello, C. Doss, K. Hunt-Stone, and J. R. Cary, Experimental opportunities for the ion channel laser, in *Proceedings of the 2018 IEEE Advanced Accelerator Concepts Workshop (AAC)* (IEEE, New York, 2018) pp. 1–5.
- [36] J. B. Rosenzweig, B. Breizman, T. Katsouleas, and J. J. Su, Acceleration and focusing of electrons in two-dimensional nonlinear plasma wake fields, *Phys. Rev. A* **44**, R6189 (1991).
- [37] S. Diederichs, T. J. Mehrling, C. Benedetti, C. B. Schroeder, A. Knetsch, E. Esarey, and J. Osterhoff, Positron transport and acceleration in beam-driven plasma wakefield accelerators using plasma columns, *Phys. Rev. Accel. Beams* **22**, 081301 (2019).
- [38] S. Reiche, Genesis 1.3: a fully 3d time-dependent fel simulation code, *Nucl. Instrum. Methods Phys. Res., Sect. A* **429**, 243 (1999).
- [39] X. Xu, F. Li, F. S. Tsung, T. N. Dalichaouch, W. An, H. Wen, V. K. Decyk, R. A. Fonseca, M. J. Hogan, and W. B. Mori, On numerical errors to the fields surrounding a relativistically moving particle in pic codes, *J. Comput. Phys.* **413**, 109451 (2020).
- [40] J.-L. Vay, Noninvariance of space- and time-scale ranges under a lorentz transformation and the implications for the study of relativistic interactions, *Phys. Rev. Lett.* **98**, 130405 (2007).
- [41] W. M. Fawley and J. Vay, Use of the lorentz-boosted frame transformation to simulate free-electron laser amplifier physics, *AIP Conf. Proc.* **1086**, 346 (2009).
- [42] A. Frazzitta, M. Yadav, J. Mann, A. R. Rossi, and J. B. Rosenzweig, Extreme radiation emission regime for electron beams in strong focusing ion channels and undulators, *Phys. Rev. Accel. Beams* **28**, 040703 (2025).
- [43] R. Bonifacio, L. De Salvo Souza, and B. McNeil, Emittance limitations in the free electron laser, *Opt. Commun.* **93**, 179 (1992).
- [44] Z. Huang and K.-J. Kim, Solution to the initial value problem for a high-gain FEL via van kampen’s method, *Nucl. Instrum. Methods Phys. Res., Sect. A* **475**, 59 (2001).
- [45] K.-J. Kim, Three-dimensional analysis of coherent amplification and self-amplified spontaneous emission in free-electron lasers, *Phys. Rev. Lett.* **57**, 1871 (1986).
- [46] L. H. Yu, S. Krinsky, and R. L. Gluckstern, Calculation of universal scaling function for free-electron-laser gain, *Phys. Rev. Lett.* **64**, 3011 (1990).
- [47] M. Xie, Exact and variational solutions of 3D eigenmodes in high gain FELs, *Nucl. Instrum. Methods Phys. Res., Sect. A* **445**, 59 (2000).
- [48] P. Baxevanis, R. D. Ruth, and Z. Huang, General method for analyzing three-dimensional effects in free-electron laser amplifiers, *Phys. Rev. ST Accel. Beams* **16**, 010705 (2013).
- [49] D. W. Peaceman and H. H. Rachford, Jr., The numerical solution of parabolic and elliptic differential equations, *J. Soc. Ind. Appl. Math.* **3**, 28 (1955).
- [50] A. M. Sessler, D. H. Whittum, and L.-H. Yu, Radio-frequency beam conditioner for fast-wave free-electron generators of coherent radiation, *Phys. Rev. Lett.* **68**, 309 (1992).
- [51] X. Xu, F. Li, F. S. Tsung, K. Miller, V. Yakimenko, M. J. Hogan, C. Joshi, and W. B. Mori, Generation of ultrahigh-brightness pre-bunched beams from a plasma cathode for x-ray free-electron lasers, *Nat. Commun.* **13**, 3364 (2022).
- [52] X. L. Xu, F. Li, W. An, T. N. Dalichaouch, P. Yu, W. Lu, C. Joshi, and W. B. Mori, High quality electron bunch generation using a longitudinal density-tailored plasma-based accelerator in the three-dimensional blowout regime, *Phys. Rev. Accel. Beams* **20**, 111303 (2017).
- [53] F. Li, T. N. Dalichaouch, J. R. Pierce, X. Xu, F. S. Tsung, W. Lu, C. Joshi, and W. B. Mori, Ultrabright electron bunch injection in a plasma wakefield driven by a superluminal flying focus electron beam, *Phys. Rev. Lett.* **128**, 174803 (2022).
- [54] B. Hidding, G. Pretzler, J. B. Rosenzweig, T. Königstein, D. Schiller, and D. L. Bruhwiler, Ultracold electron bunch generation via plasma photocathode emission and acceleration in a beam-driven plasma blowout, *Phys. Rev. Lett.* **108**, 035001 (2012).
- [55] F. Li *et al.*, Generating high-brightness electron beams via ionization injection by transverse colliding lasers in a plasma-wakefield accelerator, *Phys. Rev. Lett.* **111**, 015003 (2013).
- [56] T. N. Dalichaouch, X. L. Xu, F. Li, A. Tableman, F. S. Tsung, W. An, and W. B. Mori, Generating high quality ultrarelativistic electron beams using an evolving elec-

- tron beam driver, *Phys. Rev. Accel. Beams* **23**, 021304 (2020).
- [57] C. Joshi *et al.*, Plasma wakefield acceleration experiments at FACET II, *Plasma Phys. Controlled Fusion* **60**, 034001 (2018).
- [58] V. Yakimenko *et al.*, FACET-II facility for advanced accelerator experimental tests, *Phys. Rev. Accel. Beams* **22**, 101301 (2019).
- [59] DLMF, *NIST Digital Library of Mathematical Functions*, <https://dlmf.nist.gov/>, Release 1.1.12 of 2023-12-15, f. W. J. Olver, A. B. Olde Daalhuis, D. W. Lozier, B. I. Schneider, R. F. Boisvert, C. W. Clark, B. R. Miller, B. V. Saunders, H. S. Cohl, and M. A. McClain, eds.